3-1-2023

Two-dimensional nanomaterials confined single atoms: New opportunities for environmental remediation

Yu Yin

Lei Shi

Shu Zhang

Xiaoguang Duan

Jinqiang Zhang

See next page for additional authors

Authors

Yu Yin, Lei Shi, Shu Zhang, Xiaoguang Duan, Jinqiang Zhang, Hongqi Sun, and Shaobin Wang
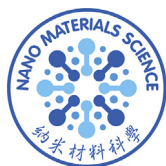
Two−dimensional nanomaterials confined single atoms: New opportunities for environmental remediation

Yu Yin [a], Lei Shi [b,*], Shu Zhang [b], Xiaoguang Duan [c], Jinqiang Zhang [c], Hongqi Sun [d], Shaobin Wang [c,**]

[a] *School of Environmental and Chemical Engineering, Jiangsu University of Science and Technology, Zhenjiang, 212100, China*
[b] *Joint International Research Laboratory of Biomass Energy and Materials, College of Materials Science and Engineering, Nanjing Forestry University, Nanjing, 210037, China*
[c] *School of Chemical Engineering and Advanced Materials, The University of Adelaide, Adelaide, SA, 5005, Australia*
[d] *School of Science, Edith Cowan University, Joondalup, WA, 6027, Australia*

ARTICLE INFO

ABSTRACT

Two−dimensional (2D) supports confined single−atom catalysts (2D SACs) with unique geometric and electronic structures have been attractive candidates in different catalytic applications, such as energy conversion and storage, value−added chemical synthesis and environmental remediation. However, their environmental applications lack of a comprehensive summary and in−depth discussion. In this review, recent progresses in synthesis routes and advanced characterization techniques for 2D SACs are introduced, and a comprehensive discussion on their applications in environmental remediation is presented. Generally, 2D SACs can be effective in catalytic elimination of aqueous and gaseous pollutants via radical or non−radical routes and transformation of toxic pollutants into less poisonous species or highly value−added products, opening a new horizon for the contaminant treatment. In addition, in−depth reaction mechanisms and potential pathways are systematically discussed, and the relationship between the structure−performance is highlighted. Finally, several critical challenges within this field are presented, and possible directions for further explorations of 2D SACs in environmental remediation are suggested. Although the research of 2D SACs in the environmental application is still in its infancy, this review will provide a timely summary on the emerging field, and would stimulate tremendous interest for designing more attractive 2D SACs and promoting their wide applications.

1. Introduction

Ever−growing world population stimulates great demands for agricultural and industrial products, which inevitably lead to enormous emission of various pollutants into the environment. These toxic substances, including dyes, pharmaceuticals, endocrine−disrupting chemicals (EDCs), poisonous inorganic gases, and volatile organic compounds (VOCs), pose severe threats to human beings and the ecological environment [1,2]. On one hand, the organic contaminants even at low concentrations are dangerous to living organisms due to the high toxicity and long−term persistence, which are easily accumulated through the food chain. As widely investigated, ~20% of incurable biological health diseases are related to these organic pollutants and heavy metal ions [3]. On the other hand, gaseous pollutants of NO_x, SO_x, and H_2S can lead to severe environmental hazards, e.g., acid rain, ozone layer destruction and photochemical smog [4,5]. For example, the 50% lethal concentration value of NO_2 is ~174 ppm within 60 min, while the maximum SO_2 concentration is around 50–100 ppm for the exposure of 30–60 min. Regarding VOCs, they are usually released from oil gas evaporation and industrial processes. Because of their easy evaporation at ambient conditions, the leaked VOCs into the atmospheric environment would cause serious health crises such as pathogenic, mutagenic and even fatal diseases [6,7].

In view of the huge danger arising from these concerned pollutants, it is highly desirable and urgent to economically eliminate the toxic species from aqueous and atmospheric environment as well as soil, realizing highly−efficient environmental remediation. Until now, various approaches have been developed to remove or transform these pollutants,

---

including physical flocculation, coagulation, sedimentation, biodegradation, and advanced catalytic degradation and conversion [8–11]. However, these traditional methods such as biodegradation and physical treatments could not thoroughly remove the highly toxic and bio-refractory contaminants, and sometimes introduce secondary pollution into the ecosystem. As an alternative, advanced catalytic degradation and conversion are considered as powerful approaches to eliminate the refractory pollutants or transfer them into less toxic species or value−added products, attracting enormous interest recently [12–16].

Due to crucial roles in the advanced catalytic reactions, versatile and promising catalysts with attractive chemical textures and unique electronic structures primarily contribute to catalytic performance. In the past decade, single atom catalysts (SACs) have received extensive attention in heterogeneous catalysis, and achieved impressive breakthroughs [17–19]. For traditional metal nanoparticles, only the exposed atoms on the outer surface are available for the reactants to be further participation in the interfacial reactions, while the enclosed atoms are not accessible to the reagents. As a comparison, each metal atom within SACs could theoretically serve as an active center, significantly maximizing the atomic efficiency, and reducing the usage cost, especially for noble metal−based catalysts. For stable and highly active SACs, the selection of proper supports for the atomic dispersion of active species to avoid their aggregation is of critical importance, in view of the remarkably increased surface energy with decreased dimensions. To this end, various supports including carbon materials, functional metal oxides, and transition metal dichalcogenides (TMDs) have been designed and developed for anchoring mono−dispersed atoms [20–23]. Normally, the appropriate supports with desirable binding sites, e.g., diverse vacancies, doped heteroatoms (N, S and P), and the surface functional groups (−OH and −COOH), are essential for the formation of specific metal−support binding, leading to the generation of highly stabilized single atoms on the supports.

Among these supports with distinct morphologies, such as one−dimensional (1D) nanowire and nanotube, two−dimensional (2D) nanosheet and nanoflake, and three−dimensional (3D) mesoporous and macroporous structures, 2D supports have demonstrated prominent and unique advantages for broad applications [24]. 2D materials, such as graphene, graphitic carbon nitride (g−C$_3$N$_4$), layered double hydroxides (LDHs), and MXenes have attracted enormous interest in energy conversion and storage, sensing, adsorption and purification [25–27]. Ascribed to the impressive properties, 2D materials themselves are extensively applied for various catalytic processes [28]. Taking functional graphene as an example, the edges, defects, or dopants within the framework could participate in catalysis, and its thin−layer structure with tunable layers provides sufficient active sites for interfacial reactions [29–31]. More importantly, the unique electronic and geometric structure of 2D materials could remarkably regulate the catalytic activity of anchored active species due to underlying metal−support interactions. Stimulated by these indelible advantages, 2D materials have been extensively applied as promising candidates for immobilization of highly dispersed metal atoms [32]. Through the formation of strong covalent binding, these metal atoms are generally stabilized by the unique coordination environment or into the lattice of 2D materials. The resultant intensive electronic interactions between the anchored single atoms and 2D supports induce the formation of new electronic states, leading to the generation of active centers with excellent catalytic properties.

2D SACs possess several unique features compared with their 1D and 3D counterparts [33,34]. Firstly, the laminar structure with tunable layers supplies a high surface area and sufficient binding sites (e.g., the defects) to anchor metal atoms, tremendously facilitating a high metal content. Meanwhile, attributed to the open structure with an easy accessibility on both sides, 2D supports could not only enhance the interfacial mass−transfer rate, but also theoretically enable a ~100% atom exposure for the reactions, remarkably boosting the catalytic efficiencies. While for 3D supports, particularly with mesoporous structures, the confined single atoms within the pores are not easily available for

interfacial catalysis in aqueous systems. Moreover, due to the vacant basal plane on both sides, the coordinatively unsaturated single atoms are generally more active to achieve a higher catalytic performance. In addition, the uniform atomic and electronic structures of single atoms on 2D supports can be precisely investigated by advanced characterization approaches, in contrast to these of 1D and 3D supports. For example, the aberration−corrected high−angle annular dark−field scanning transmission electron microscopy (AC−HAADF−STEM) is a typical 2D projection technique to analyze single atoms on the catalysts along the direction of the incident beam [35]. Therefore, for these 3D support−based samples, the acquired atomic images cannot fully reflect actual atom dispersion due to possible overlapped structures. Last but not least, the simple structures of 2D supports, as well as the uniform coordination states of the loaded single atoms, make the 2D SACs proper candidates for model construction and theoretical exploration, providing a pivotal tool to probe underlying reaction pathways and mechanisms. As a consequence, the emergence and rapid development of 2D SACs have shed new light for both theoretical investigations and experimental studies of advanced catalysis.

Up to now, a series of reviews on SACs have been reported, focusing on their applications in energy conversion and storage, catalytic hydrogenation, medicine and environmental remediation via thermocatalysis, electrocatalysis and photocatalysis [36–38]. While most of the reviews for 2D support−based SACs primarily deal with the energy conversion and storage [39–41]. For example, Bao et al. summarized three typical 2D materials of graphene, g−C$_3$N$_4$, and MoS$_2$ as the supports for the loading of single atoms, and introduced various catalytic applications in hydrogenation reactions, oxygen reduction/evolution reaction (ORR/OER), CO$_2$ reduction reaction (CRR), and water splitting reaction [40]. Yin et al. updated the recent synthesis methods for 2D SACs, and systematically discussed their electrochemical energy storage applications in rechargeable batteries, such as Li–CO$_2$, Li–O$_2$ and Li–S batteries [41]. With the rapid development in the 2D SACs, their huge potential and impressive merits for environmental remediation receive ever−−growing attentions recently. However, few reviews focusing on this aspect are reported up to now. Moreover, apart from the classical 2D materials, new emerging 2D candidates, such as graphdiyne (GDY), have aroused great interest for anchoring single atoms [42,43]. For instance, GDY only possesses sp and sp^2 hybridized carbon atoms within adjacent benzene rings connected by the diacetylenic linkages (−C≡C–C≡C−). Different from the traditional single atom bonding mode on carbon supports, active single atoms could be stabilized on GDY through the formation of strong d–π interaction with the –C≡C– structure. Meanwhile, with the rapid development of nanotechnology and science, new synthesis approaches have been developed recently. Bearing these considerations in mind, it is highly desired to update the recent progress of 2D SACs, and summarize their advantages for the highly−concerned environmental remediation.

In this review, we first summarize the emerging applications of 2D SACs in environmental remediation (Fig. 1). The review starts from the introduction of synthesis strategies for anchoring various single atoms into 2D supports, and then the approaches toward identification of active sites in the 2D supports are introduced and compared. Subsequently, the catalytic applications of 2D SACs in different environmental remediation processes are comprehensively discussed. In particular, the review will unveil the relationship between the structure−catalytic performances of 2D SACs, and discuss the underlying catalytic mechanisms for pollutant decomposition and transformation. Eventually, the present challenges and future prospective in this important field are provided.

2. Synthesis strategies for 2D SACs

For highly−efficient and scale applications of 2D SACs, developing facile and reliable synthesis routes is prerequisite. Generally, versatile synthesis strategies mainly including chemical vapor deposition (CVD), atomic layer deposition (ALD), high−temperature pyrolysis, wet
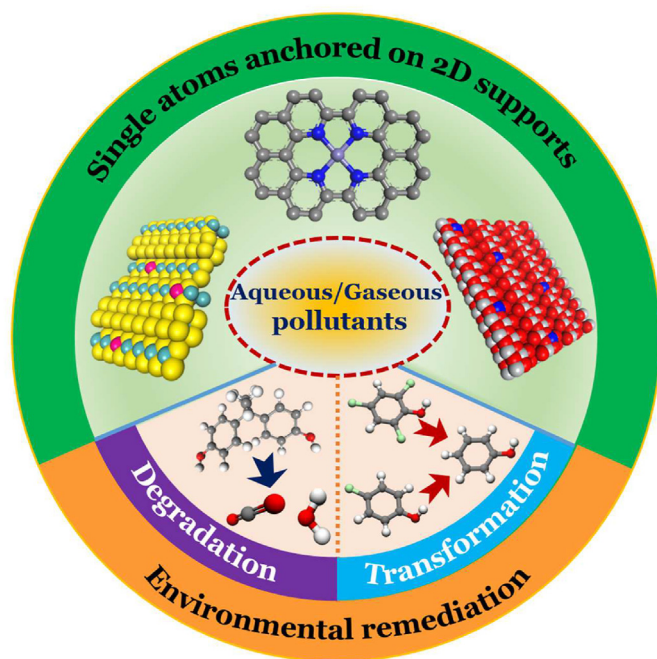
Fig. 1. Construction and application of 2D SACs for environmental remediation.

impregnation, and photo/electrochemical reduction have been widely adopted for the preparation of 2D SACs. Apart from these familiar approaches, emerging methods such as ball−milling strategy and cocoon silk chemistry method are also discussed in this section.

2.1. CVD and ALD routes

As the most popular vapor growth technology and reliable bottom−up method, CVD is extensively used for the preparation of 2D materials (e.g., graphene, metal oxide and TMDs), and various SACs [44–46]. During a typical CVD process, precursors are firstly converted into volatile species with assistance of a heat treatment. Carrying with a flowing gas, gaseous precursors are captured by the available surface sites, undergoing further chemical reactions on the supports to achieve the controllable growth of nanomaterials. Liu et al. successfully incorporated Co single atoms (Co SAs) into a MoS$_2$ support, through substituting Mo atoms with the CVD route [47]. The Co loading into the MoS$_2$ lattice was effectively regulated via regulating the molar ratio of S powder, MoO$_3$, and CoCl$_2$ (Fig. 2a). The scanning transmission electron microscopy−annular dark−field (STEM–ADF) images confirmed the successful doping of Co SAs into the support, displaying clearly Mo atoms (brighter) and S column (dimmer). Moreover, the obtained electron energy loss spectroscopy (EELS) analysis within individual metal sites also demonstrated the substitution of Mo with Co into the MoS$_2$ lattice (Fig. 2b).

Comparable with CVD technique, ALD is well known for its precise deposition of uniform and conformal thin films on supports, following controllable atomic layer−by−layer manners [48,49]. Undergoing the diffusion of precursor vapors, subsequent adsorption and final interfacial reaction, this approach is suitable for various supports with distinct dimensions and morphologies. For the construction of 2D SACs, Sun et al. recently utilized this method for the load of Pt SAs on an oxygen functionalized graphene [50]. Exposing with the Pt−containing precursor of MeCpPtMe$_3$, the limited surface oxygen on the graphene reacted with the partial ligands in the precursor, resulting in self−limiting growth to produce one atomic Pt layer. The following oxygen exposure generated an additional adsorbed layer on Pt surface, completing an ALD cycle. Through adjusting ALD cycles, the density and loading amount of Pt on the graphene support could be effectively controlled. Inspired by this
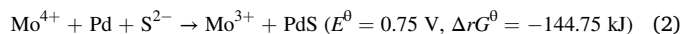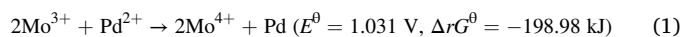
work, Lu et al. firstly synthesized Pd SAs on graphene with a similar procedure, utilizing palladium hexafluoroacetylacetate (Pd(hfac)$_2$) as the precursor [51]. To construct high−quality single atoms on graphene with the ALD technique, the graphene supports with desirable functional groups as anchor sites are highly anticipated. To this end, oxidation and subsequent thermal deoxygenation were performed to generate isolated phenol groups for anchoring Pd(hfac)$_2$, through the generation of –O–Pd–hfac structures (Fig. 2c). After removing residual hfac ligands through the formalin exposure, isolated Pd SAs were successfully confined on the graphene, as confirmed by the AC−HAADF−STEM (Fig. 2d).

Compared with these vapor diffusion approaches, a comparable solid−state diffusion strategy, involving the migration of solid−state atoms or the transformation of bulk metals into single atoms, has been developed for the synthesis of 2D SACs [52,53]. Utilizing the breakage of the metal−metal bond within the bulk metals/particles by a heat treatment or thermal oxidation, separated single atoms were generated and subsequently trapped on the supports through this top−down synthesis route. More specific details of this promising approach were systematically introduced in a previously reported review [54].

These diffusion approaches display unique merits for the synthesis of excellent SACs, due to the controllable and accurate manipulation at the atomic level, especially with ALD. However, the high cost and complicated operation procedures, as well as the special requirements to the supports, would hinder their widespread applications in practice.

2.2. Wet impregnation

In contrast to the above vapor/solid−state diffusion approaches, wet impregnation is more attractive and widely adopted for the synthesis of SACs, through immersing the supports in the metal−precursor solution with the presence/absence of reductants. For example, Pd SAs/g−C$_3$N$_4$ and Fe SAs/GDY were successfully constructed using PdCl$_2$ and FeCl$_3$ as the metal precursors, respectively, and NaBH$_4$ as the reductant [58,59]. Alternatively, utilizing the underlying redox or coordination interactions, self−reduction or anchoring is realized to achieve an efficient construction of single atoms on the supports without any reductant, providing a promising route for the facile and ecofriendly synthesis of 2D ASCs. As a paradigm, Ge et al. proposed a thermodynamically spontaneous redox reaction between MoS$_2$ and Pd^{2+} to synthesize Pd SAs on 2D MoS$_2$ [55]. A chemically synthesized MoS$_2$ (the atomic Mo:S = 1:1.87) with a lower valence state of Mo (~3.74) displayed an intensive redox capacity. Following the favorable process depicted in Eq. (1), Pd was reduced accompanying with the oxidation of Mo, generating Mo vacancies due to charge conservation (Fig. 2e). Located at the energetic Mo vacancies, the resultant Pd was anchored into a MoS$_2$ framework via the formation of stable Pd–S bond, as depicted in Eq. (2).

$$2Mo^{3+} + Pd^{2+} \rightarrow 2Mo^{4+} + Pd \ (E^\theta = 1.031 \text{ V}, \Delta rG^\theta = -198.98 \text{ kJ}) \quad (1)$$

$$Mo^{4+} + Pd + S^{2-} \rightarrow Mo^{3+} + PdS \ (E^\theta = 0.75 \text{ V}, \Delta rG^\theta = -144.75 \text{ kJ}) \quad (2)$$

MXenes, unique 2D metal carbides, nitrides, and carbonitrides, display huge potentials in catalysis and energy storage applications [60], and have attracted increased interest in the construction of 2D SACs. Recently, Chen et al. reported the preparation of stabilized single atoms on ultrathin Ti$_{3-x}$C$_2$T$_y$ nanosheets, through a similar self−reduction process [56]. Ti$_{3-x}$C$_2$T$_y$ nanosheets displayed several attractive merits. First of all, each Ti$_{3-x}$C$_2$T$_y$ layer consisted of three Ti sub−layers, while the adjacent layers were connected with a reactive Al layer. The exfoliation treatment through etching the Al layer partially removed Ti atoms simultaneously. Thus, the produced unstable and reactive Ti vacancies made the reductive MXene nanosheets competent candidates for the reduction of metal precursors, in the absence of additional reductants (Fig. 2f). Meanwhile, after the deletion of Al layers, the resultant functional groups (e.g., OH$^-$ and F$^-$) were beneficial for the electrostatic adsorption of metal precursors, thus facilitating the subsequent reduction
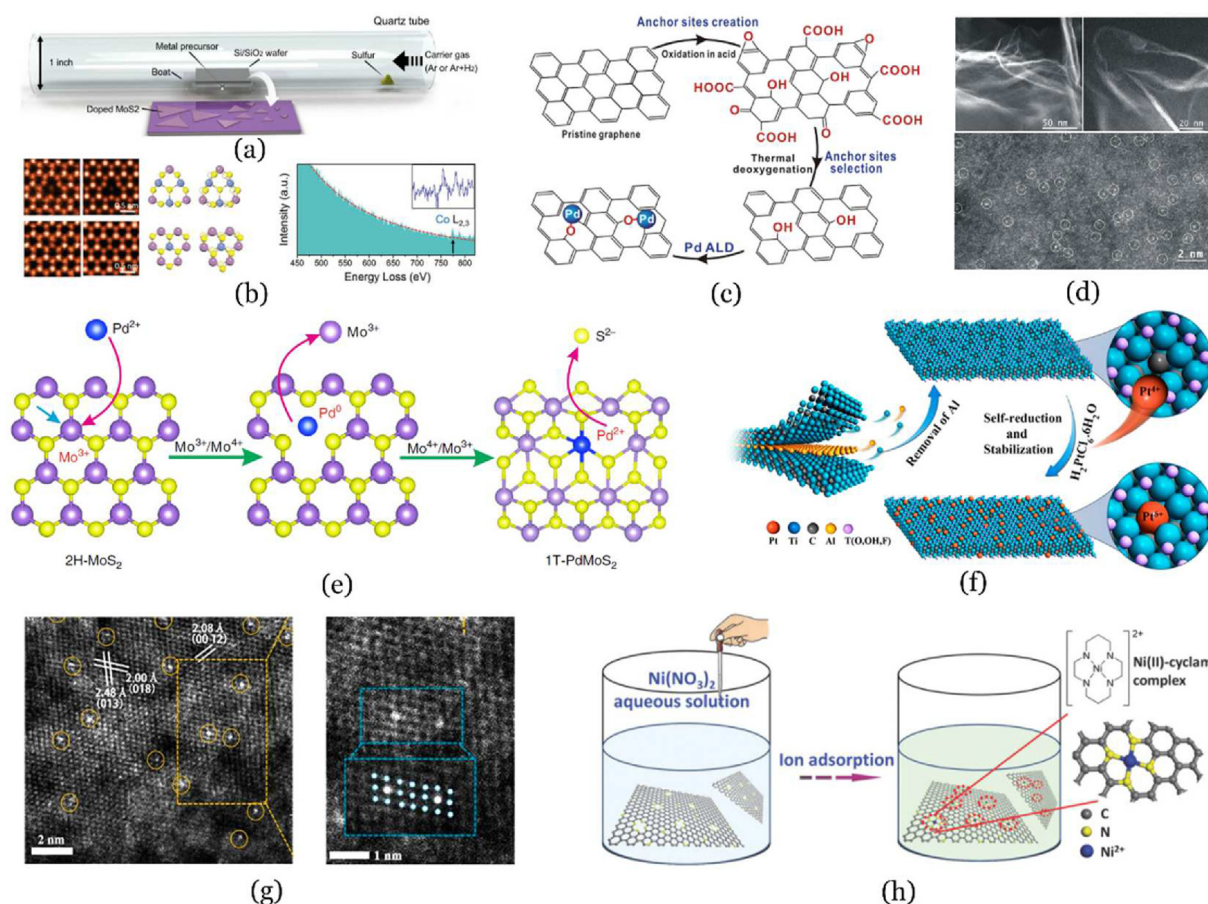
Fig. 2. (a) The CVD setup applied for preparation of Co−doped MoS$_2$. (b) Atom−resolved STEM−ADF images, simulated STEM images and corresponding single−−atom EELS analysis of Co−doped MoS$_2$ [47]. Reproduced with permission: Copyright 2020, Wiley−VCH Verlag GmbH & Co. KGaA, Weinheim. (c) Schematic illustration for the preparation of Pd$_1$/graphene through an ALD route. (d) HAADF−STEM images of constructed Pd$_1$/graphene [51]. Reproduced with permission: Copyright 2015, American Chemical Society. (e) Schematic illustration of the formation process of Pd/MoS$_2$ [55]. Reproduced with permission: Copyright 2018, Springer Nature. (f) Illustration of the fabrication procedure for the Pt$_1$/Ti$_{3−x}$C$_2$T$_y$. (g) HAADF−STEM images of Pt$_1$/Ti$_{3−x}$C$_2$T$_y$ [56]. Reproduced with permission: Copyright 2019, American Chemical Society. (h) Schematic illustration of the Ni^{2+} stabilization onto N−doped graphene [57]. Reproduced with permission: Copyright 2018, Wiley−VCH Verlag GmbH & Co. KGaA, Weinheim.

of single atoms. Furthermore, the surface defects could serve as the suitable anchoring sites for single atoms, significantly enhancing the stability of 2D SACs. The atomic−resolution HAADF−STEM image of Pt$_1$/Ti$_{3−x}$C$_2$T$_y$ verified the uniformly dispersed Pt atoms (small bright dots in the yellow circles) within lattice fringes of the Ti$_{3−x}$C$_2$T$_y$ support (Fig. 2g). More importantly, this preparation strategy could be easily extended to the fabrication of a series of SACs, including Ru, Ir, Rh, and Pd.

Apart from these TMDs and MXenes, functional graphene also demonstrated the applicability in the wet impregnation route for single atom loading. Wu et al. adopted a simple ion adsorption route to immobilize Ni^{2+} on N−doped graphene, followed by mild annealing to improve the stability [57]. Different from the CVD route or post−doping treatment with graphene oxide, the N−doped graphene with ultrathin nanosheets was prepared via the pyrolysis of g−C$_3$N$_4$ and glucose mixture. The resultant N−doped graphene selectively supplied sufficient pyridinic−N to capture Ni SAs, forming the cyclam−like macrocycles within the graphene framework (Fig. 2h).

Despite impressive advantages of wet impregnation strategy for the construction of 2D SACs, several challenges are still remained. For example, special requirements toward 2D supports, such as suitable trapping sites as well as matched redox capacities, would definitely hamper the widespread applications. Besides, the loading amount and binding strength of single atoms are required to be further improved.

Therefore, it is highly anticipated to develop universal approaches for the efficient synthesis of 2D SACs.

2.3. High−temperature pyrolysis strategy

Amongst diverse approaches for the preparation of 2D SACs, pyrolysis treatment is regarded as one of mostly universal routes. Adopting metal salts, C/N containing sources (e.g., melamine, dicyandiamide), or other inorganic/organic materials (e.g., graphene oxide, metal organic frame-work−MOF) as the precursors, 2D supports (normally graphene or carbon) confined single atoms were extensively fabricated in the absence/ presence of functional templates [61–63].

Song et al. reported an in−situ pyrolysis route for the preparation of high−loading single atoms (e.g., Pt and Fe) on N−doped graphene (Fig. 3a), using a mixture of inorganic metal salt, glucose, and dicyan-diamide as the precursors [64]. Compared with the post−treatment routes, strong chemical interactions within the metal species and carbon precursors were favorable and critical to achieve enhanced stabilization of single atoms and high loading of metals (e.g., 9.26 wt% for Pt SAs). Anchoring into the framework of 2D graphene nanosheets, the highly dispersed single atoms (e.g., Pt SAs, Fig. 3b) were observed in the HAADF−STEM images. Similarly, through an efficient chelation between glucose and Fe ions, and subsequent formation of physically isolated glucose–Fe complexes with excessive glucose, Fe SAs with a high metal
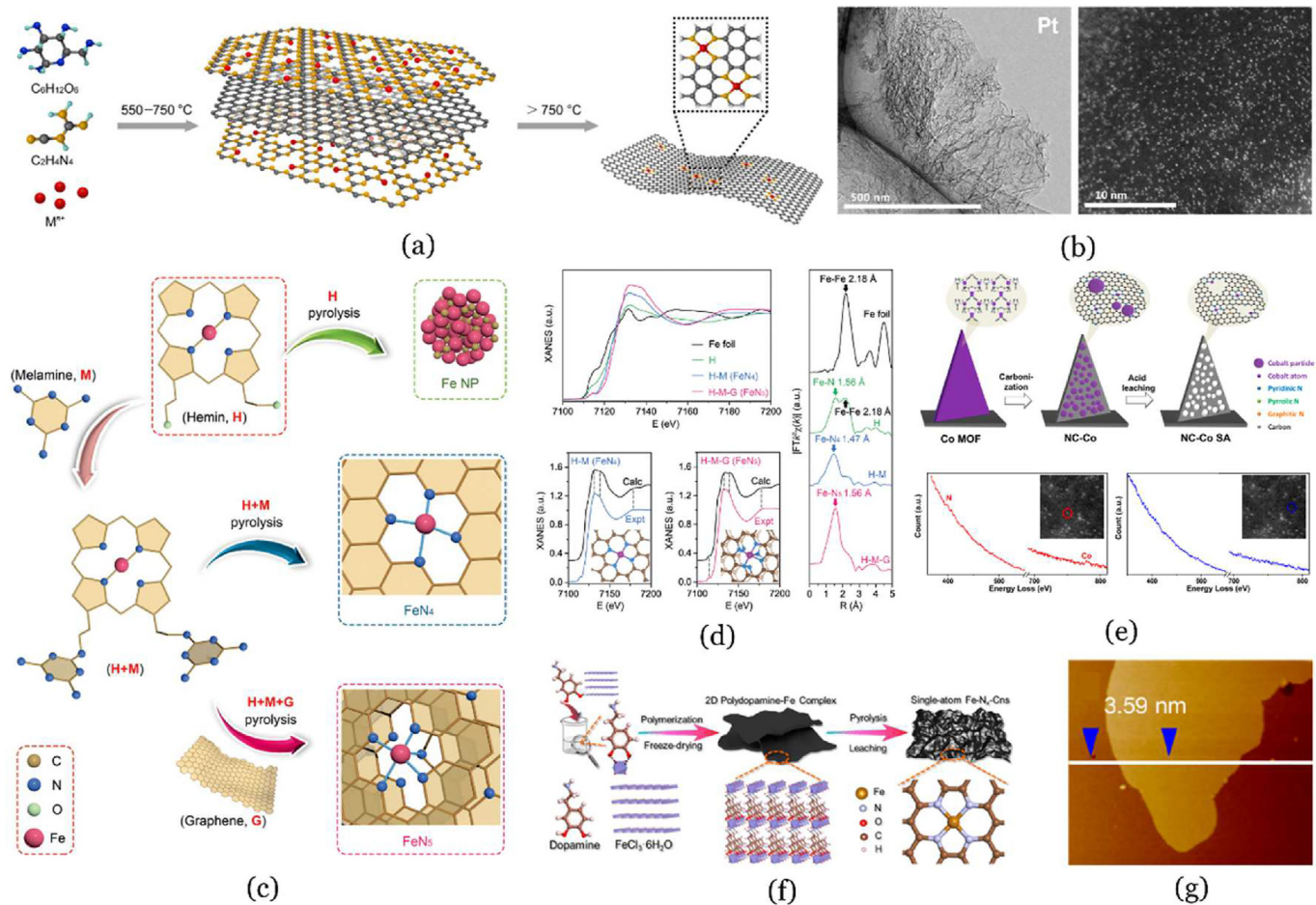
Fig. 3. (a) Schematic synthesis approach for single atoms anchored N−doped graphene. (b) Representative TEM and HAADF−STEM images of Pt SAs/N−doped graphene [64]. Reproduced with permission: Copyright 2018, Tsinghua University Press and Springer−Verlag GmbH Germany, part of Springer Nature. (c) Proposed approaches for the construction of 2D SACs containing FeN$_4$ and FeN$_5$ centers. (d) Fe K−edge XANES and EXAFS spectra of various catalysts [66]. Reproduced with permission: Copyright 2019, Wiley−VCH Verlag GmbH & Co. KGaA, Weinheim. (e) Illustration of fabrication procedure and related EELS spectra of NC−Co SAC nanoflake [67]. Reproduced with permission: Copyright 2018, American Chemical Society. (f) Schematic synthesis of Fe−N$_x$−Cns. (g) Atomic force microscopy (AFM) image with thickness profile of Fe−N$_x$−Cns [16]. Reproduced with permission: Copyright 2020, American Chemical Society.

loading (~12.1 wt%) were successfully anchored on N–doped carbon sheets after the pyrolysis treatment [65]. Inspiringly, through forming an enhanced interaction between metal species and carbon precursors in advance, this ingenious strategy could not only significantly contribute to a high loading amount of single atoms, but also effectively hinder the formation of large particles.

Utilizing a similar pyrolysis route, Wang et al. reported the preparation of Fe SAs on N–doped graphene, and effectively adjusted the active sites (e.g., FeN$_4$, FeN$_5$) through the addition of defective graphene [66]. In contrast to Fe nanoparticles generated with the direct pyrolysis of Hemin, the internal cross−linking of melamine and Hemin effectively suppressed Fe atom aggregation, creating Fe SAs via the formation of FeN$_4$ on graphene (Fig. 3c). Importantly, the introduction of defective graphene induced the formation of sufficient N−doped graphene, and offered additional axial ligands for the coordination of FeN$_4$, resulting in the creation of desirable FeN$_5$ catalytic sites for an enhanced CRR. As the most effective approaches to reveal the atomic coordination structures, X−ray absorption near edge structure (XANES) characterization, extended X−ray adsorption fine structure (EXAFS) spectra, as well as the density functional theory (DFT) simulation, confirmed the presence of two types of Fe SAs (FeN$_4$ and FeN$_5$) in the graphene framework (Fig. 3d). Inspiringly, this work sets a paradigm for the oriented construction of SACs with tunable coordination environment.

Apart from above−mentioned precursors, diverse MOF materials

with excellent properties in heterogeneous catalysis, adsorption and separation, and energy storage [68–72], have demonstrated as promising precursors for the construction of various functional materials on account their structure and composition diversity. In view of both metal sites and organic linkers co−existed within MOF materials, the pyrolysis of MOF−based composites would generally produce highly porous graphitized carbon−based nanomaterials [73]. In the past few years, the adoption of MOF−based precursors for the synthesis of SACs has aroused enormous interest [74–76]. Particularly for those 2D MOFs after the pyrolysis treatment, atomically distributed metal centers would be transformed into single atoms while the organic linkers could be converted into carbon nanosheets, retaining their initial 2D morphologies [77,78]. For instance, Guan et al. designed a carbonization−acidification route for the construction of Co SAs embedded into N−doped carbon nanoflake (NC−Co SA, Fig. 3e). In addition to the preservation of lamellar structure, both Co and N signals in the EELS spectra of the resultant 2D NC−Co SA confirmed the formation of sufficiently stable Co−N$_x$ structure [67].

However, ascribed to the high surface energy within carbon nanosheets during the high temperature calcination, the crumpled and even agglomerated structures instead of desired 2D laminar configurations tend to be formed. To this end, various templates (e.g., hard MgO and soft NaCl templates) were introduced for the preparation of SACs with well−defined 2D morphologies [79–81]. For instance, Li et al. fabricated

Fe SAs on ultrathin carbon nanosheets (Cns, Fe$-$N$_x$$-$Cns) utilizing a salt$-$template polymerization approach, following by freeze$-$drying and subsequent pyrolysis [16]. As depicted in Fig. 3f, abundant FeCl$_3$·6H$_2$O crystals not only served as the laminar template, but also accelerated the polymerization of dopamine hydrochloride with the oxidation performance of Fe^{3+}. After a freeze$-$drying treatment to reduce the surface tension, the obtained inorganic$-$organic hybrid with the layered structure was calcined to produce the Fe$-$N$_x$$-$Cns (thickness of ~3.59 nm, Fig. 3g).

As the mostly adopted strategy for the construction of 2D SACs, the pyrolysis pathway is favorable for anchoring a high amount of metal sites onto diverse supports. Nevertheless, desirable uniform 2D structures with the controllable dispersion of single atoms remain as a challenge. Moreover, the adopted high pyrolysis temperature would induce the agglomeration of metal species, and additional acid etching treatment is thus required for removing large particles.

2.4. Photo/electrochemical reduction approach

Driven by powerful light or electrical energy, emerging photochemical or electrochemical reduction approaches attract enormous attention for the construction of 2D SACs [82–84]. The capacity toward redox reactions could be effectively regulated by the imposed light irradiations with various wavelengths and intensities, or the applied potentials on the electrodes. Especially for the electrochemical approach, size and amount of deposited nanomaterials could be accurately regulated through varying applied current density or the potential, adopting a proper ionic concentration or pH value, and optimizing deposition time or cycle.

As an attempt of electrochemical reduction for the construction of 2D SACs, Wang et al. successfully deposited Pt SAs on MXene (Mo$_2$TiC$_2$T$_x$) nanosheets [82]. Firstly, Mo$_2$TiC$_2$Tx nanosheets were electrochemically exfoliated, inducing the generation of abundant surface Mo vacancies for the immobilization of Pt SAs dissolved from the counter Pt electrode (Fig. 4a). Through the formation of covalent Pt$-$C/O bonds (Fig. 4b), Pt SAs were exactly immobilized at the Mo positions on Mo$_2$TiC$_2$Tx, as demonstrated in the magnified HAADF$-$STEM image (Fig. 4c).

Moreover, Zhou et al. reported a universal cathodic/anodic deposition strategy to produce over 30 kinds of SACs (e.g., Ru, Rh, Pd, Ag, Pt, etc.) through varying metal precursors and supports [83]. Taking Ir SAs deposited on Co(OH)$_2$ nanosheets for an example, IrCl$_6^{3+}$ cations approached the cathode surface driven by the imposed electric field, and were subsequently reduced on the support (Fig. 4d). Through the coordination with three O atoms of Co(OH)$_2$ support, C–Ir$_1$/Co(OH)$_2$ with highly dispersed Ir atoms on Co(OH)$_2$ support was acquired (Fig. 4e). While for the anodic deposition, Ir(OH)$_6^{2-}$ anions were adopted for the synthesis of A–Ir$_1$/Co(OH)$_2$ following a similar procedure. Confirmed with the EXAFS spectra, the absence of Ir–Ir contribution of Ir$_1$/Co(OH)$_2$ demonstrated the feasibility of both cathodic/anodic deposition for the synthesis of SACs. Intriguingly, these SACs with the same metal synthesized by different routes exhibited different electronic states, and thus displayed distinct behaviors for catalyzing hydrogen evolution reaction (HER) and OER, providing an efficient approach for the depth investigation of the relationship between structure$-$performance.

As for the photochemical reduction, the process normally involves absorption of photons, excitation of photo$-$induced active species, and subsequent redox reaction with various precursors to obtain the products. For example, atomically dispersed Pt SAs were successfully synthesized via iced$-$photochemical reduction [84]. Treated in liquid nitrogen, an ice layer with a homogeneously dispersed Pt precursor was formed to prevent atom aggregation, followed by the subsequent reduction under UV irradiation (Fig. 4f). Comparably, Zheng et al. proposed a room$-$temperature photochemical strategy for in$-$situ synthesis of highly stable Pd SAs on TiO$_2$ nanosheets (Pd$_1$/TiO$_2$) [85]. TiO$_2$ nanosheets (~two$-$atom thickness) stabilized with the ethylene glycolate (EG) were applied as the functional support to immobilize Pd SAs, via the formation of robust Pd–O structure. As for such kind of synthesis system, an efficient elimination of residual Cl$^-$ ligands attached on the catalyst surface is essential to acquire high catalytic performance. Interestingly, the EG derived –OCH$_2$CH$_2$O• radicals under UV irradiation effectively promoted the removal of Cl$^-$ ligands on Pd surface, leading to the generation of highly active Pd SAs.

Compared with the electrochemical reduction approach with a relative broad universality, the photochemical method toward the reduction of other metals on different supports is deserved to be explored in future.
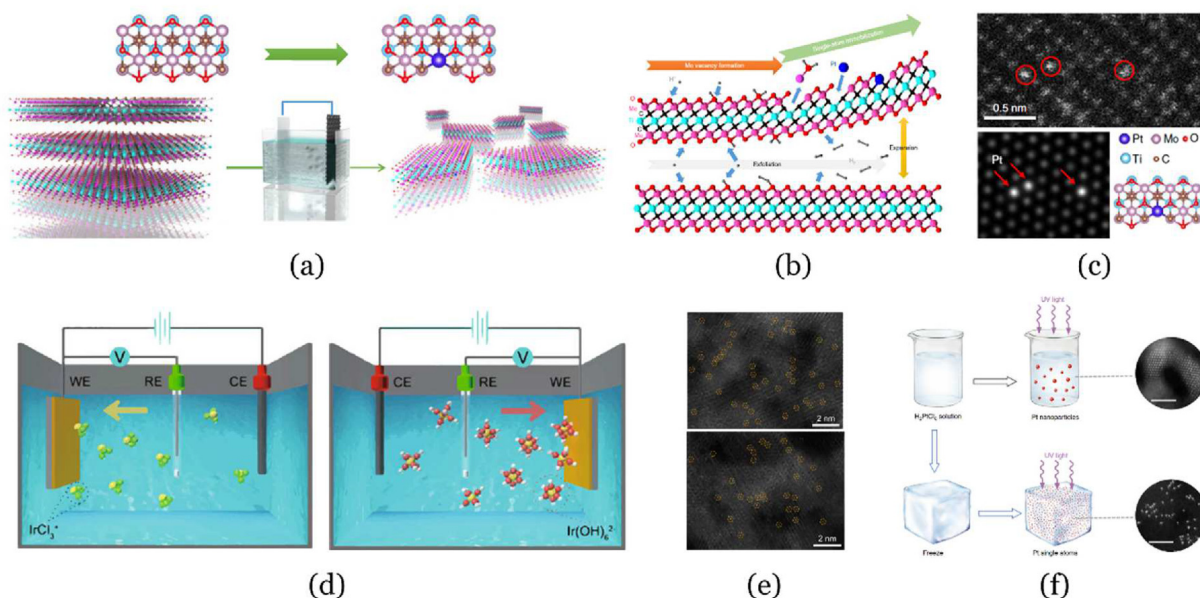
Fig. 4. (a) Schematic illustration, and (b) corresponding mechanism of the electrochemical synthesis of Pt SAs on Mo$_2$TiC$_2$T$_x$. (c) Magnified HAADF$-$STEM image, and related simulated image of Pt SAs/Mo$_2$TiC$_2$T$_x$ [82]. Reproduced with permission: Copyright 2018, Springer Nature. (d) Schematic illustration of cathodic (left) and anodic (right) deposition setup for the preparation of Ir–based SACs. (e) HAADF$-$STEM images of C–Ir$_1$/Co(OH)$_2$ (top) and A–Ir$_1$/Co(OH)$_2$ (below) [83]. Reproduced with permission: Copyright 2020, Springer Nature. (f) Schematic illustration of the iced$-$photochemical procedure [84]. Reproduced with permission: Copyright 2017, Springer Nature.

Meanwhile, although the photo/electrochemical reduction routes are mild for the controllable preparation of SACs, the mass production is remained as a great challenge and unflagging efforts are required to further improve the synthesis efficiency. Furthermore, an efficient removal of residual ligands attached on the formed single atoms is urgently requisite to acquire highly active sites.

2.5. Other emerging methods

Apart from the above familiar approaches, other emerging methods including ball−milling strategy, and cocoon silk chemistry approach were also developed for the fabrication of 2D SACs [86]. Utilizing the formed intensive shear force and high temperature within the ball−milling procedure, Bao et al. reported a general route for the preparation of several 2D graphene based SACs [87]. Through ball−milling of graphene and metal phthalocyanines under Ar atmosphere, metal precursors were decomposed and active single atoms were firmly embedded into the graphene framework, via the formation of robust metal−N_4 structures. Based on this attractive approach, Mn, Fe, Co, Ni and Cu SAs were effectively stabilized on the 2D graphene support.

As for the cocoon silk chemistry approach, it is inspired by laminar sheet structures of silk fibroin, with abundant amino groups on the surface for the tight anchoring of metal precursors [88]. Four steps were generally involved in this strategy, including degumming of cocoons, regeneration of silk fibroin, metal salt−participated pyrolysis, and acid etching treatment. Following the pyrolysis treatment, porous carbon nanosheets were produced, along with the conversion of amino groups into N species doped into carbon framework for the stabilization of various single atoms (e.g., Fe, Co and Ni).

In this section, popular synthesis strategies for the construction of single atoms on 2D supports are systematically summarized and discussed. Each strategy displays unique merits and disadvantages as well. The proper supports, desirable metal species, as well as the potential applications should be taken into consideration in screening an appropriate strategy. From the perspective of remaining challenges, including cost, scale−up, and controllable regulation toward a high loading content, there is huge room to further optimize and improve the aforementioned strategies for the construction of 2D SACs. With the rapid development in the field of nanomaterial and nanoscience, it is highly anticipated that more attractive approaches would be developed for the highly−effective fabrication of 2D SACs.

3. Identification and characterization of the active sites within 2D SACs

In revealing the pivotal relationships between the structure−catalytic performances of designed 2D SACs, an accurate identification toward the active sites and their coordination environment, as well as the operando monitoring of their chemical property and structure evolutions during the reactions, are highly anticipated and imperative.

Up to now, a series of advanced characterization tools have been established for a deep investigation into the chemical and electronic structures of SACs (Fig. 5). In this section, several representative techniques, including scanning tunneling microscopy (STM) [89], STEM [90], X−ray absorption spectroscopy (XAS) [91], X−ray photoelectron spectroscopy (XPS) [92], and other familiar techniques (e.g., Fourier−transform infrared spectroscopy) and theoretical tools (e.g., DFT simulations) [93], are introduced and discussed.
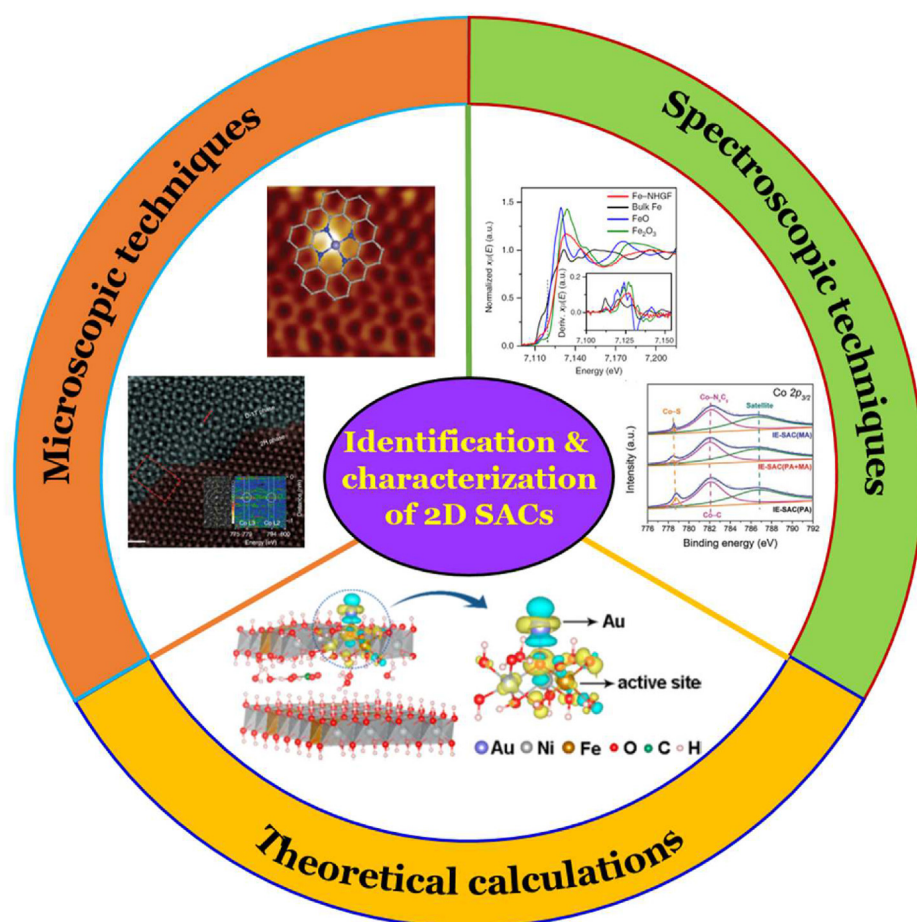
Fig. 5. Representative techniques and tools for the identification and characterization of 2D SACs, mainly including STM [89], Reproduced with permission: Copyright 2015, The American Association for the Advancement of Science, AC−HAADF−STEM [90], Reproduced with permission: Copyright 2019, Springer Nature, XAS [91], Reproduced with permission: Copyright 2018, Springer Nature, XPS [92], Reproduced with permission: Copyright 2020, Wiley−VCH Verlag GmbH, and DFT simulation [93], Reproduced with permission: Copyright 2018, American Chemical Society.

3.1. Microscopic techniques

In verification of the absence of nanoparticles and the presence of laminar morphologies of synthesized catalysts, TEM or high−resolution TEM (HRTEM) characterizations are generally performed for the preliminary estimation. Once receiving the positive feedback, further measurements, such as AC−HADDF−STEM, are recommended for capturing the images of the single atoms at the atomic levels. Avoiding the overlapped projection of active sites within the irregular supports, more precise structural details could be obtained on ultrathin 2D materials.

As the surface−science technique, STM has been broadly applied for the structure analysis of catalysts with flat structure [94]. Ascribed to the ultrahigh resolution at an atomic scale, STM can even distinguish slight changes on the geometric and electronic structures. Taking N doped graphene as an example, the N position with close atomic numbers could be identified with STM [95]. Recently, the electronic and atomic structures of Fe SAs on graphene were explored with low−temperature STM. As depicted in the inset in Fig. 5, the brighter dots of Fe atom and surrounding N atoms than these C atoms in graphene implied the significant alteration toward the density of electronic states (DOS) of adjacent C or N atoms after the anchoring of Fe SAs [89]. Located in the basal plane of graphene, the formed FeN_4 structure was eventually confirmed by the STM image. As the complementary technique to TEM characterization, STM analysis could provide more precise structural information of SACs.

Moreover, as a powerful technique for surface imaging, AFM is applied for the measurement of various forces, such as adhesion strength and magnetic forces [96]. In spite of few reports focusing on the identification of single atoms with AFM, it offers an efficient approach to achieve critical information on the surface textures, including thickness, morphology, and roughness. For instance, ultrathin carbon nanosheet (thickness of ~3.59 nm) and defective monolayer graphene (thickness of 0.4–0.6 nm) were confirmed for the loading of Fe SAs [16,97].

3.2. Spectroscopic techniques

Despite the indispensable roles in the characterization of 2D SACs with these microscopic techniques, it should be recognized that the acquired results could not conclusively exclude the possibility of existed nanoparticles, because only limited sections of the catalysts are examined by the microscopic techniques. To this end, various spectroscopic techniques have been developed for further verification of the atomic dispersion of single atoms on supports. Normally, X−ray diffraction (XRD) is initially performed to determine the absence of nanoparticles, according to the corresponding peaks of these metal species. Meanwhile, energy dispersive X−ray spectroscopy (EDX) is conducted to confirm the existence of metal elements on the surface of supports.

To acquire more in−depth details toward the chemical structure and coordination environment of single atoms on supports, XAS tests have been extensively conducted to provide more precise and direct evidences. The XAS is consisted of two sections, including the XANES and EXAFS [98,99]. The critical information like the electronic structure and coordination state of single atoms could be obtained with the XANES, through comparing these typical peaks and shoulders near or on the edges of XAS. While for the EXAFS, the average inter−atomic distance and local coordination number between anchored single atoms and the adjacent backscatter atoms may be deduced accordingly to understand the geometric configurations. As a direct evidence for the formed SACs, the absent signal on the metal–metal bonding in the EXAFS spectra could thus demonstrate only isolated metal atoms in the catalyst.

For example, in contrast to that of Fe foil, the edge of XANES spectra of both FeN_4 and FeN_5 samples shifted toward higher binding energy, indicating a positive charge state of Fe SAs in the catalyst (Fig. 3d) [66]. The atomic structures (e.g., FeN_4 and FeN_5) were demonstrated with the DFT simulations coupling with a standard XANES calculation. Moreover, the dominant peaks centered at ~1.47 Å (FeN_4) and 1.56 Å (FeN_5) within the Fourier transformed (FT) extended EXAFS confirmed the existence of isolated Fe SAs, without the Fe–Fe peak located at ~2.18 Å.

In addition to the pivotal XAS technique, other approaches like X−ray photoelectron spectroscopy (XPS) and infrared (IR) spectroscopy are also applicable for the identification of active sites within SACs [92]. Apart from the determination of surface composition, XPS could be used for the illustration of the valence states of metal species from the high-−resolution narrow spectra, which could be employed for the structural differentiation of single atoms and nanoparticles. For example, the peak of pyridinic N bonding with single atoms would generally shift to higher binding energy, via the formation of metal−N_x sites anchored on a graphene support [100,101]. In addition, FT−IR technique is another effective tool to identify the amount of single−atom species on the supports. Through monitoring the vibrational intensity and frequency of probe molecules, the surface properties of catalysts could be acquired. For example, in−situ FT−IR is extremely sensitive to the vibrations of adsorbed CO molecules, thus offering the distinct evidences for discriminating the single atoms (e.g., Ir, Rh and Pt) from their counterparts like the clusters or nanoparticles [19,102,103].

3.3. Theoretical calculation and prediction for SACs

In addition to the experimental characterizations, computational explorations, e.g., DFT simulation, have been extensively applied for the study of 2D SACs and possess several unique advantages. Firstly, the simple and uniform structures of 2D SACs make them suitable candidates for a reliable theoretical exploration. Meanwhile, theoretical calculations offer an efficient analysis toward the electronic structures of the active sites, which are critical for the construction of descriptors to determine the catalytic activity, selectivity, as well as stability of SACs [104,105]. Generally, the energy (e.g., Gibbs free energy) and structure (e.g., metal−N_x or metal−C_xN_y) descriptors are extensively adopted for the description of catalytic performance. Moreover, computational simulation provides an attractive approach for the deeper understanding into possible reaction pathways and mechanisms, thus offering a feasible tool to uncover the structure–performance relationship.

In virtue of the DFT calculations, the catalytic properties for several critical reactions on SACs were systematically studied and predicted, including familiar CRR, OER/ORR, nitrogen reduction reaction (NRR), selective hydrogenation and dehalogenation, as well as advanced oxidation processes (AOPs) [106–110]. Taking the electrocatalytic reaction for an example, the activity of SACs is normally dependent on the potential−determining step (PDS), which is determined by the maximum change in the Gibbs free energy during the reaction process. The PDS reflects the degree of difficulty and the possible bottleneck for the reaction with the constructed SACs. With the rapid development of theoretical techniques, it is extremely anticipated that advanced computational methods would open new avenues for the in−depth and accurate explorations into reaction mechanisms, and guide the rational design of attractive and promising catalysts for wider applications.

Overall, in the prosperous field of SACs, an efficient integration of versatile characterization techniques and simulation approaches is generally recommended for the confirmation of single atoms, the exploration of critical active centers, and the revelation of possible reaction pathways. Recently, emerging in−situ monitoring techniques have attracted enormous interest, on account of their timely and accurate understanding toward the potential structure and property variations on catalysts during catalytic reactions [111,112]. Stimulated by these merits, developing and establishing effective operando characterization tools for SAC−participated reactions are highly anticipated and urgent in future.

4. Environmental remediation by 2D SACs

With the rapid development of SACs, their applications in the environmental remediation have received enormous interests, as summarized in Table 1. Amongst the representative supports, 1D N−doped carbon

Table 1
Various support−based SACs for environmental remediation applications.

Support		Metal specie	Synthesis method	Application	Ref.
1D	N−doped CNT	Fe−N$_4$ (5.81 wt%)	Pyrolysis	Bisphenol A (BPA) degradation	[117]
	N−doped CNT	Co−N$_x$ (/)	Pyrolysis + Acid washing	BPA degradation	[118]
	TiO$_2$ nanowire	Pt−O$_x$ (0.2 wt%)	Microwave−assisted dip−coating	Diesel oxidation	[119]
	N−doped CNT	Co−N$_4$ (0.01 wt%)	Pyrolysis + Acid washing	Sulfamethoxazole (SMX) degradation	[120]
	Mn$_2$O$_3$ nanowire	Ag (0.06 wt%)	Molten salt method	Toluene removal	[121]
	OMS nanotube	Pt (0.0383 wt%)	Wet impregnation	Benzene oxidation	[122]
	WO$_3$/TiO$_2$ nanotube	Au (2.41 wt%)	Electrochemical deposition	Toluene removal	[123]
2D	Lamellar porous carbon	Fe−N$_4$ (1.23 wt%)	CVD + Acid leaching	SMX degradation	[124]
	N−doped rGO	Cu−N$_4$ (/)	Pyrolysis	SMX degradation	[125]
	N−doped wrinkled carbon	Fe−N$_4$ (5 wt%)	Pyrolysis + Acid washing	2,4−Dichlorophenol degradation	[126]
	MoS$_2$	Fe−S$_x$ (13.8 wt%)	Hydrothermal route	Propranolol degradation	[127]
	N−doped carbon sheet	Fe−N$_4$ (1.85 wt%)	Pyrolysis + Acid leaching	Dechlorination of 1,2−dichloroethane	[16]
	rGO	Ni−O$_x$ (/)	Wet impregnation	4−Nitrophenol to 4−aminophenol	[128]
	Carbon doped boron nitride (BCN) sheet	Co−N$_3$ (1.4 wt%)	Pyrolysis	Dechlorination of chloramphenicol	[129]
	MgO nanosheet	Pt−O$_4$ (0.47 wt%)	Wet impregnation	Toluene oxidation	[130]
3D	Mesoporous Fe$_2$O$_3$	Pt−O$_x$ (0.25 wt%)	Wet impregnation + Calcination	Benzene combustion	[131]
	TiO$_2$ hollow microsphere	Fe−Ti$_x$/Fe−O$_x$ (0.58 wt%)	Pyrolysis	NO oxidation to NO$_3^-$	[132]
	NH$_2$−UiO−66/MnO$_2$	Ru−N$_x$ (0.63 wt%)	Wet impregnation	NO$_x$ oxidation to NO$_x^-$	[133]
	N−doped porous biochar	Cu−N$_4$ (3.41 wt%)	Pyrolysis	BPA degradation	[134]
	N−doped porous carbon	Mn−N$_4$ (0.27 at%)	Pyrolysis	BPA degradation	[135]
	N−doped porous carbon	Fe−N$_4$ (0.61 wt%)	CVD	Phenol degradation	[136]
	N−doped porous carbon	Fe−N$_4$ (0.57 wt%)	Pyrolysis + Acid washing	Phenol degradation	[137]
	N−doped porous carbon	Fe−N$_x$ (3.92 wt%)	Pyrolysis	BPA degradation	[138]
	Defective porous carbon	C$_3$−Fe−Cl$_2$ (2.23 wt%)	Pyrolysis + Acid washing	SMX degradation	[139]
	Mesoporous silica nanosphere	Rh−N(O)$_x$ (4.3 wt%)	Wet impregnation	4−Nitrophenol to 4−aminophenol	[140]
	Nanoporous TiO$_2$ film	Pt−O$_x$ (/)	Wet impregnation + Thermal reduction	Toluene removal	[141]
	N−doped porous carbon	Pd−N$_x$ (~1.71 wt%)	Pyrolysis + Acid washing	Dechlorination of 4−chlorophenol	[142]

nanotube (CNT) and metal oxide nanowires (e.g., TiO$_2$ and Mn$_2$O$_3$), 2D N−doped carbon nanosheets, N−doped rGO and TMDs, and 3D N−doped porous carbon and meso/microporous metal oxides (e.g., Fe$_2$O$_3$ and TiO$_2$) have been extensively adopted for the immobilization of various single atoms. Regardless of the type of supports, the universal pyrolysis method as well as wet impregnation approach are widely applied for the synthesis of desirable SACs. For the environmental remediation, two main aspects such as pollutant elimination and transformation have been explored with fantastic SACs. Notably, the carbon−based supports immobilized with transition metals (e.g., Fe, Co, Cu and Ni) are mostly adopted for the treatment of aqueous contaminants, while metal oxi−de−based supports confined noble metals (e.g., Pt, Ag and Au) are generally constructed for the elimination of gaseous pollutants.

Serving as heterogeneous catalysts to trigger diverse AOPs for removing various pollutants, SACs are superior candidates to produce highly active radicals (e.g., HO•, SO$_4^{•-}$ or O$_2^{•-}$) and non−radical species (e.g., ^{1}O$_2$), through (i) the activation of various oxidants, such as H$_2$O$_2$, peroxymonosulfate (PMS), peroxydisulfate (PDS) or sulfite; (ii) photo-catalysis, or electrocatalysis, as well as (iii) coupled photo−PMS, pho-to−PDS or photo−H$_2$O$_2$ routes [36,113,114]. While for the pollutant transformation, dechlorination and hydrogenation reduction reactions have been established with SACs for the elimination of highly toxic pollutants or the production of value−added intermediates.

As for 2D SACs, they possess several unique merits and hold great potentials for environmental remediation applications. In addition to serving as the supports for loading of different single atoms, 2D supports could also offer sufficient active sites on both planes for the generation of reactive species, extensively boosting the catalytic activities as the co−catalysts. Meanwhile, attributed to the potential π–π stacking in-teractions, these easily acquired carbon supports (e.g., graphene, porous carbon, g−C$_3$N$_4$) could boost the adsorption of aromatic compounds, realizing an enhanced degradation or transformation of environmental pollutants [115,116]. Upon the immobilization of various single atoms onto 2D supports, the resultant synergetic interactions would trigger the generation of abundant active sites, affording diverse reaction routes for the subsequent elimination and transformation. Thus, in the following section, we will focus on a systematical introduction into environmental applications of 2D SACs, discuss underlying reaction mechanisms and

pathways, and reveal the potential relationship between the structure−performance.

4.1. Elimination of aqueous environmental pollutants

4.1.1. H$_2$O$_2$−based degradation

Due to its acceptable operation cost, and environmental friendliness with low toxicity, homogenous Fenton or heterogeneous Fenton−like reaction has been extensively applied for the elimination of aqueous refractory contaminants, utilizing Fe−based catalysts for H$_2$O$_2$ activation to generate highly reactive HO• [143–145]. However, for the traditional Fe−based catalysts, the challenges remain as a low activation rate and narrow working pH range. To this end, enormous Fe−based SACs like Fe SAs/SBA−15, and Fe SAs/g−C$_3$N$_4$−graphitized mesoporous carbon were developed to achieve higher activities or wider working pH windows for the boosted removal of p−hydroxybenzoic acid (HBA), phenol and Acid Red 73 [146,147].

Comparable to the Fe−based species, active Cu sites could efficiently induce H$_2$O$_2$ reduction to easily generate HO•. For example, through a facile pyrolysis of a mixture of Cu−melamine complex, GO and cyanuric acid, Li et al. synthesized Cu SAs on N−doped GO (Cu−SA/NGO) to stimulate the Fenton−like process [148]. Owing to the unique ligand−-field effect, CuN$_4$ sites facilitated the cleavage of H$_2$O$_2$ into reactive HO• and a hydroxyl group (OH*) in the rate−determining step, displaying a significantly reduced lower energy barrier (1.45 eV) than that of NGO (3.01 eV) in both acidic and neutral media (Fig. 6a). In view of that OH* interacted with H$^+$ via hydrogen bonding in the acidic condition, the subsequent desorption of formed H$_2$O induced the surface regeneration of the catalyst. As a comparison, OH* species combined with H$_2$O$_2$ under the neutral condition (Fig. 6b), generating the HO$_2$* with a lower oxidation ability than that of OH*. Accordingly, a superior performance toward degradation of paracetamol (APAP) at lower pH conditions was achieved on Cu−SA/NGO (Fig. 6c).

In addition to the Fenton−like processes, HO• could be spontane-ously produced through the peroxone reaction (H$_2$O$_2$ + O$_3$). However, the low activity toward HO• formation in acidic solution severely pre-vented its broad−field application [149,150]. To address this issue, Mn SAs anchored on 2D g−C$_3$N$_4$ were designed to effectively activate the
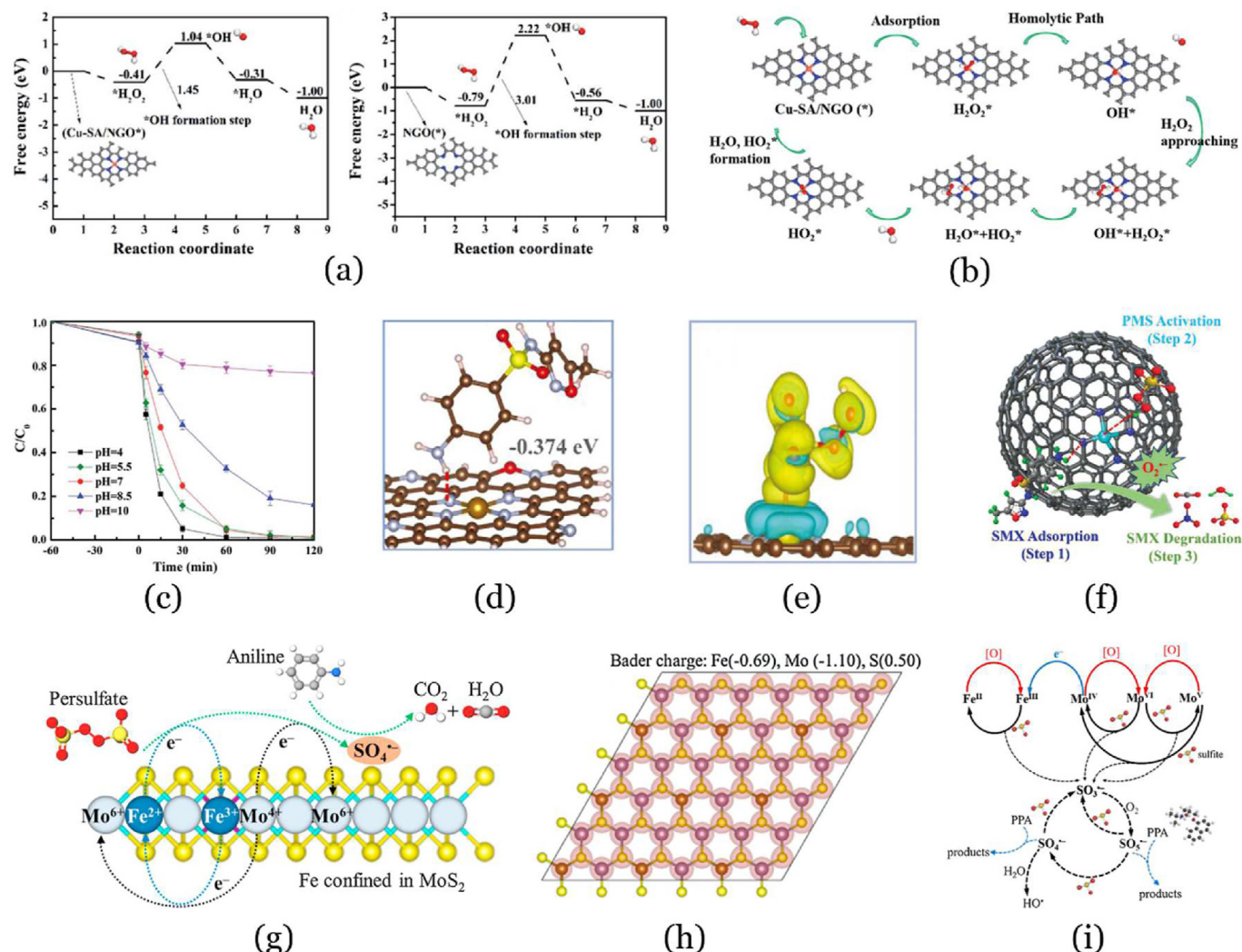
Fig. 6. (a) Corresponding free−energy diagrams on Cu−SA/NGO and NGO. (b) Mechanism of Cu−SA/NGO participated Fenton−like reaction under neutral condition. (c) Effects of pH on APAP degradation [148]. Reproduced with permission: Copyright 2020, Royal Society of Chemistry. (d) Adsorption simulation of amino group on FeN$_4$−graphene. (e) Charge density distribution between PMS and FeN$_4$. (f) Degradation mechanism of the FeN$_4$−PC/PMS system [124]. Reproduced with permission: Copyright 2021, Wiley−VCH GmbH. (g) The mechanism of aniline elimination in Fe$_x$Mo$_{1−x}$S$_2$/PDS system. (h) Charge density and Bader charge transfer of atoms in Fe$_x$Mo$_{1−x}$S$_2$ [152]. Reproduced with permission: Copyright 2020, Elsevier. (i) The involved sulfite activation mechanism on Fe$_x$Mo$_{1−x}$S$_2$ catalyst [127]. Reproduced with permission: Copyright 2019, Elsevier.

peroxone reaction under acidic condition, achieving a quick generation of HO• via the consecutive reactions [151]. Comparably with CuN$_4$ sites on NGO, MnN$_4$ sites accelerated the adsorption of H$_2$O$_2$ to form the HOO–MnN$_4$ species, which further interacted with O$_3$ to rapidly produce HO$_2^•$ and O$_3^{•−}$. The HO$_2^•$ was firstly converted to O$_2^{•−}$ that subsequently reacted with O$_3$ to produce O$_3^{•−}$. Via the combination with H$^+$, O$_3^{•−}$ was rapidly transformed into HO$_3^•$, eventually converting to desirable HO•. Taking the advantage of active HO• radicals, 2D Mn SAs/g−C$_3$N$_4$ demonstrated a superior degradation activity for the removal of oxalic acid, outperforming its counterpart of a homogeneous Mn^{2+} catalyst.

For most H$_2$O$_2$−based AOPs, current concerns are primarily focused on the design of highly active catalysts for H$_2$O$_2$ activation. Nevertheless, another fundamental challenge of AOPs for in−situ H$_2$O$_2$ production has received few attentions. To this end, Cui et al. coupled a H$_2$O$_2$ electrolyzer and a Fenton filter in tandem, and developed a low energy and chemical required system for highly−efficient treatment of organic wastewater [153]. For the upstream H$_2$O$_2$ electrolyzer, on−site generation of H$_2$O$_2$ from air and water was realized by the 2e−ORR, using the electrocatalyst of oxidized Super P carbon black. While for the downstream Fenton filter, Cu SAs anchored g−C$_3$N$_4$ (Cu SAs/g−C$_3$N$_4$) with the

unique single−electron redox capacity would favor the robust radical route over non−radical pathway for the H$_2$O$_2$ activation. Accordingly, the Cu SAs/g−C$_3$N$_4$ demonstrated an efficient pollutant elimination with active HO• species, superior to that of CuO nanoparticles/g−C$_3$N$_4$. Compared with the two components in tandem, a bi−functional 2D SAC was constructed through anchoring Co SAs onto S and N doped graphene (Co SAs/SNG) to achieve the consecutive production and activation of H$_2$O$_2$ within the same system [154]. The doped heteroatoms with higher electronegativity and surface oxygen−containing functional groups facilitated O$_2$ adsorption, while highly dispersed Co–N–C active sites contributed to the 2e−ORR for an efficient H$_2$O$_2$ generation. Together with the in−situ formation of sufficient HO•, a complete degradation (~91.1%) of inorganic molecules was achieved on the Co SAs/SNG catalyst. Coupling the production and activation of H$_2$O$_2$, these pioneering researches not only motivate technological advancements within the AOPs, but also enable convenient and efficient environmental remediation in remote regions.

4.1.2. Sulfate oxidant−based degradation
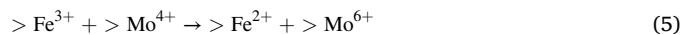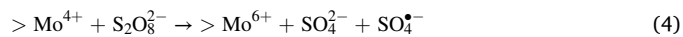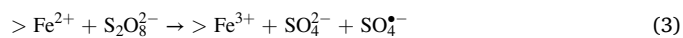
Apart from H$_2$O$_2$ participated Fenton−like reactions, oxysulfur

radicals (e.g., $SO_4^{\bullet-}$, $SO_5^{\bullet-}$) participated AOPs deriving from the activation of PDS, PMS or sulfite have received enormous interest for the elimination of diverse organic pollutants in recent years [155–159]. In contrast to HO• (e.g., 1.8–2.7 V vs. NHE, 20 ns), $SO_4^{\bullet-}$ radicals possess higher oxidation potentials (e.g, 2.5–3.1 V vs. NHE) and durable half−life periods (e.g., 30–40 μs), displaying superior and attractive oxidation capacities. More importantly, the activation toward PMS or PDS could be realized with various metal or metal−free based catalysts in a broad pH range, making these processes possible for large−scale applications [160].

Accompanying with the generation of oxysulfur radicals, the formation of other active species, such as HO• and $O_2^{\bullet-}$, are widely observed. These radical−based routes, coupling with non−radical pathways, enable high efficiencies for the pollutant removal [161]. Different with the unselective radical oxidation procedure, non−radical participated oxidation is generally active towards specific contaminants. Taking Co SAs stabilized on curled N−doped carbon sheets (Co SAs/NC) for example, Co SAs induced the radical generation from PMS activation, while N doped carbon framework accounted for non−radical PMS activation [162]. Interestingly, the radical reaction contributed to the removal of benzotriazole (BTZA) and diatrizoate (DTZ), while the non−radical (not the traditional $^1O_2$) reaction significantly dominated the degradation of 5−benzoyl−4−hydroxy−2−ethoxybenzenesulfonic acid (BP−4) and 2,4−dichlorophenol (2,4−DCP). Attributed to impressive mixed reaction routes, the Co SAs/NC demonstrated a superior activation capacity toward PMS than homogenous Co^{2+} system.

As well known, the diverse dopants and their unique coordination environment within the carbon−based supports induce the change of local electronic structures, leading to a synergetic effect to boost the elimination efficiency toward pollutants. For instance, Pen et al. successfully stabilized Fe SAs into N doped laminar C structures utilizing a CVD method, and explored its activity for PMS activation to remove SMX [124]. The N and Fe sites within the formed FeN₄–C structure were confirmed as dual active centers. Through the van der Waals force, the N atom in FeN₄–C structure enhanced SMX adsorption with the shortened H–N distance (1.999 Å), possessing stable adsorption energy of −0.374 eV (Fig. 6d). Meanwhile, due to the electron migration between PMS and FeN₄ (Fig. 6e), the FeN₄ coordination significantly facilitated the chemisorption and activation of PMS on the carbon framework. Eventually, the activated $SO_4^{\bullet-}$ radicals by Fe SAs were subsequently transformed into $O_2^{\bullet-}$ and HO• to boost the degradation of SMX (Fig. 6f). Similarly, Fe−pyridinic N₄ moiety immobilized within 2D N−doped carbon laminate architecture demonstrated an unexceptionable activity for PMS activation [163]. On one hand, the electron−rich Fe atoms enabled PMS reduction to generate HO• and $SO_4^{\bullet-}$. On the other hand, the electron−poor carbon sites binding to pyridinic N not only enhanced the accessibility for PMS, but also promoted the oxidation of PMS to generate $SO_5^{\bullet-}$ with receiving electrons from PMS. The $SO_5^{\bullet-}$ radical was further transformed into $^1O_2$ with the interaction of water molecules. Meanwhile, accumulated electrons on such carbon sites streamed toward Fe sites through the Fe–N–C structure. The increased electron density of Fe SAs thus promoted the reduction of dissolved oxygen to generate $O_2^{\bullet-}$. Utilizing this unique PMS activation mechanism with simultaneous redox routes, an efficient degradation of BPA was eventually acquired.

Compared with aforementioned carbon supports, the metal compound−based supports demonstrate attractive advantages for the loading of diverse single atoms. The unique metal−support interactions, particularly the redox reaction between anchored single atoms and intrinsic metal atoms from supports, enhance the catalytic activity via synergistic effects. As an attempt, 2D MoS₂ containing Fe SAs (FeₓMo₁₋ₓS₂) was synthesized to activate PDS for aniline degradation (Fig. 6g) [152]. The incorporation of Fe atoms induced the decrease of electrons on Mo and S sites, resulting in the destabilization of the electronic structure. Meanwhile, the charge transfer (0.69 e^{-1}) amongst Fe SAs and MoS₂ confirmed a robust metal−support interaction (Fig. 6h), not only hindering the aggregation of Fe atoms but also enabling a rapid charge migration

between Fe and Mo. Consequently, the stabilized Fe SAs with a low formal oxidation state (Eq. (3)), the Mo catalytic sites (Eq. (4)), as well as the redox reactions between Fe^{2+}/Fe^{3+} and Mo^{4+}/Mo^{6+} sites (Eq. (5)), synergistically boosted the PDS activation for the continuous production of $SO_4^{\bullet-}$ radicals. Undergoing a similar activation mechanism (Fig. 6i), FeₓMo₁₋ₓS₂ nanosheets effectively mimicked the sulfite oxidase enzyme to promote sulfite activation, producing sufficient $SO_5^{\bullet-}$ as main radicals for an efficient degradation of propranolol (PPA) [127]. Compared with PMS and PDS, the sulfite has attractive merits like low toxicity and cheap synthesis route, providing an alternative route for AOPs [164].

$$> Fe^{2+} + S_2O_8^{2-} \rightarrow > Fe^{3+} + SO_4^{2-} + SO_4^{\bullet-} \qquad (3)$$

$$> Mo^{4+} + S_2O_8^{2-} \rightarrow > Mo^{6+} + SO_4^{2-} + SO_4^{\bullet-} \qquad (4)$$

$$> Fe^{3+} + > Mo^{4+} \rightarrow > Fe^{2+} + > Mo^{6+} \qquad (5)$$

In addition to MoS₂ support, this unique metal−support redox interaction is widely observed in other metal compound supports (e.g., MXenes), which significantly contributes to an enhanced activation ability. For instance, through a general defect anchoring strategy, Co SAs were tightly anchored on the Ti vacancy within 2D Ti₂₋ₓN MXene [165]. Through the activation toward PMS by Co SAs, active radicals like HO• and $SO_4^{\bullet-}$ were generated accompanying with Co oxidation. Owing to the strong reducibility of MXene support, a Co^{3+}/Co^{2+} redox cycle was triggered for continuous PMS activation to achieve a robust oxidation activity. Interestingly, the Ti₂₋ₓN support also served a crucial role as the electron shuttle for a direct electron migration between PMS and adsorbed contaminants, resulting in a non−radical oxidation pathway. The multiple radical and non−radical oxidation routes contributed to a rapid removal of SMX, 2,4−DCP and carbamazepine (CBZ).

4.1.3. Other oxidant−based degradation

Apart from above widely investigated oxidants, emerging researches focused on periodate (IO_4^-)−based AOPs have received great attention [166,167]. The formation of robust radicals (e.g., HO• and $IO_3^\bullet$) enables an efficient elimination of organic species from aquatic environments. In spite of a proper oxidation capacity of IO_4^- (~1.60 V), its activation suffers from a higher kinetic barrier. Thus, developing efficient activators to accelerate the insufficient reaction rates is considered as the core issue for the IO_4^- activation. From the perspective of SACs, Zhang et al. demonstrated the first instance of employing Co SAs supported by N−doped graphene (N−rGO−CoSA) to achieve a robust activation toward IO_4^- [168].

Compared with the familiar CoN₄, CoN₂O₂ sites facilitated the adsorption of IO₄ molecules (the lowest adsorption energy of −3.690 eV) and significantly enhanced the stretch of the I–O bond (~1.872 Å). Meanwhile, the boosted electron migration between IO₄ species and Co sites resulted in the generation of a charge−transfer complexes, e.g., the metastable Co SAs/periodate* complexes (Fig. 7a). Impressively, these metastable complexes could extract electrons from specific pollutants, along with the stoichiometric decomposition of IO_4^- to IO_3^- species (Fig. 7b). This unique electron−transfer−mediated non−radical oxidation process enabled a target−specific reactivity, realizing a selective removal of pollutants. For example, phenol and 4−chlorophenol (4−CP) with electron−donating groups were easily oxidized due to their low oxidation potentials. As a contrast, benzoic acid and carbamazepine (CAMP) with electron−withdrawing groups were difficult to be removed via the electron−transfer regime, ascribed to their high oxidation potentials. Compared with optimal N−rGO−CoSA (Fig. 7c), N−rGO−Co nanoparticles with insufficient accessible active sites displayed an inferior activation property, while Co^{2+} and nanosized Co₃O₄ nanoparticles were inactive for IO_4^-.

4.1.4. Photocatalysis−based degradation

Through the utilization of green and sustainable solar energy, photocatalysis is regarded as the environmentally friendly technology to
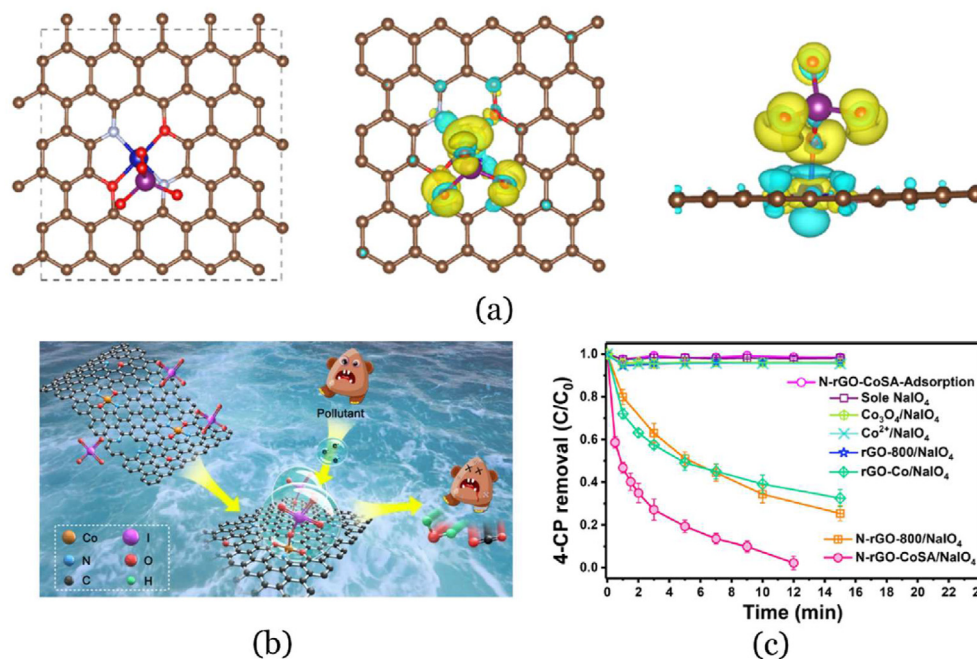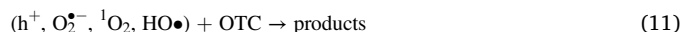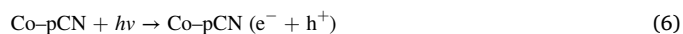
Fig. 7. (a) Adsorption configuration of IO_4^- and related charge density difference on the graphene/CoN_2O_2 model. (b) Schematic non−radical procedure for the pollutant elimination. (c) Degradation activity of 4−CP using different catalysts [168]. Reproduced with permission: Copyright 2021, American Chemical Society.

effectively address the issues arising from energy crisis and environmental contamination [169–172]. In the absence of additional chemical reagents, photocatalysts can absorb light to produce active electrons (e$^-$) and holes (h$^+$) for pollutant elimination. As it is well known, an outstanding light−harvesting ability across a broad solar light spectrum, and a prompt separation and migration of photogenerated carriers significantly contribute to an impressive photocatalytic activity of a photocatalyst.

To this end, it is urgent to develop promising photocatalysts with unique band structures and surface properties through various catalyst design strategies, such as heteroatom doping, morphology regulation and heterostructure construction [173–175]. Taking the widely adopted metal−free semiconductor, g−C_3N_4 or polymeric carbon nitride (pCN) as an example, it has attracted tremendous attention in photocatalytic pollutant degradation, as well as in energy regeneration, due to the tunable band structures, low toxicity, and excellent chemical and thermal stability [176,177]. However, the poor conductivity, low specific area, as well as the quick recombination of charge carriers, severely hinder its performance. To address this issue, engineering single atoms into the skeleton of g−C_3N_4 or pCN through the coordination interaction could significantly enhance its light absorption and charge separation properties, resulting in improved photocatalytic activities [178,179].

For this purpose, a facile in−situ growth strategy was adopted to incorporate Co SAs into 2D pCN (Co–pCN), through the formation of a bidentate ligand consisting of covalent Co–N and Co–O bonds (Fig. 8a) [180]. In contrast to pristine pCN, the anchored Co SAs significantly improved the delocalization of π system and enhanced electron transfer, displaying a boosted electron spin resonance (ESR) intensity (Fig. 8b). Meanwhile, a higher carrier recombination barrier with a decreased PL response was favorable for the separation and migration of photo−induced e$^-$–h$^+$ pairs (Eq. (6)), thus accumulating sufficient charge carriers for the subsequent photocatalytic reaction (Fig. 8c). Utilizing the active species generated within diverse routes, such as $O_2^{\bullet-}$ (Eq. (7)), $^1O_2$ (Eq. (8)), HO• (Eq. (9)−10), as well as h$^+$ (Eq. (11)), the Co(1.28%)–pCN displayed an extensively boosted photocatalytic activity for the oxytetracycline (OTC) degradation (Fig. 8d). Due to the robust chemical and structural stability, the designed photocatalyst exhibited an excellent recycle performance with a subtle activity decrease (Fig. 8e).

$$Co–pCN + h\nu \rightarrow Co–pCN\ (e^- + h^+) \tag{6}$$

$$e^- + O_2 \rightarrow O_2^{\bullet-} \tag{7}$$

$$O_2^{\bullet-} + h^+ \rightarrow {}^1O_2 \tag{8}$$

$$O_2^{\bullet-} + e^- + 2H^+ \rightarrow H_2O_2 \tag{9}$$

$$H_2O_2 + e^- \rightarrow HO\bullet + OH^- \tag{10}$$

$$(h^+, O_2^{\bullet-}, {}^1O_2, HO\bullet) + OTC \rightarrow products \tag{11}$$

In addition to the introduction of single atoms, Liu et al. designed a ternary photocatalyst through simultaneously anchoring Ag SAs and carbon quantum dots (CQDs) on a 2D ultrathin g−C_3N_4 nanosheet (SDAg−CQDs/UCN) [181]. The incorporation of CQDs and Ag SAs enabled significant positive shifts in the Fermi levels (E_f) and conduction band (CB) as well, facilitating the generation of active carriers and offering a shorter transfer path for the photo−induced electrons (Fig. 8f). Impressively, the extended light absorption from UV, visible, to near−infrared light was achieved due to the surface plasmon resonance (SPR) effect of Ag SAs, the up−converted PL properties of the CQDs, as well as the narrowed energy gap. Upon the light irradiation, photo−generated electrons were sequentially transferred from the UCN, Ag SAs to CQDs within the unique ternary heterostructure (Fig. 8g), and accumulated electrons participated in the generation of abundant radicals (e.g., $O_2^{\bullet-}$, $^1O_2$, and HO•). Ascribed to the high surface area of SDAg−CQDs/UCN, as well as intensive π–π interactions toward adsorption of naproxen (NPX), an efficient decomposition was acquired utilizing both active radicals and photo−induced h$^+$.

Stimulated by the impressive performance achieved with the oxidant (e.g., H_2O_2, PMS and PDS) participated routes, as well as the photocatalytic procedures, emerging attentions have been dedicated to the combination of these pathways to acquire tremendously boosted efficiencies in pollutant degradation [182]. Up to now, diverse coupled photo−PDS, photo−PMS, and photo−Fenton like routes have been established on various 2D SACs, and corresponding pathways toward the elimination of pollutants were systematically explored.

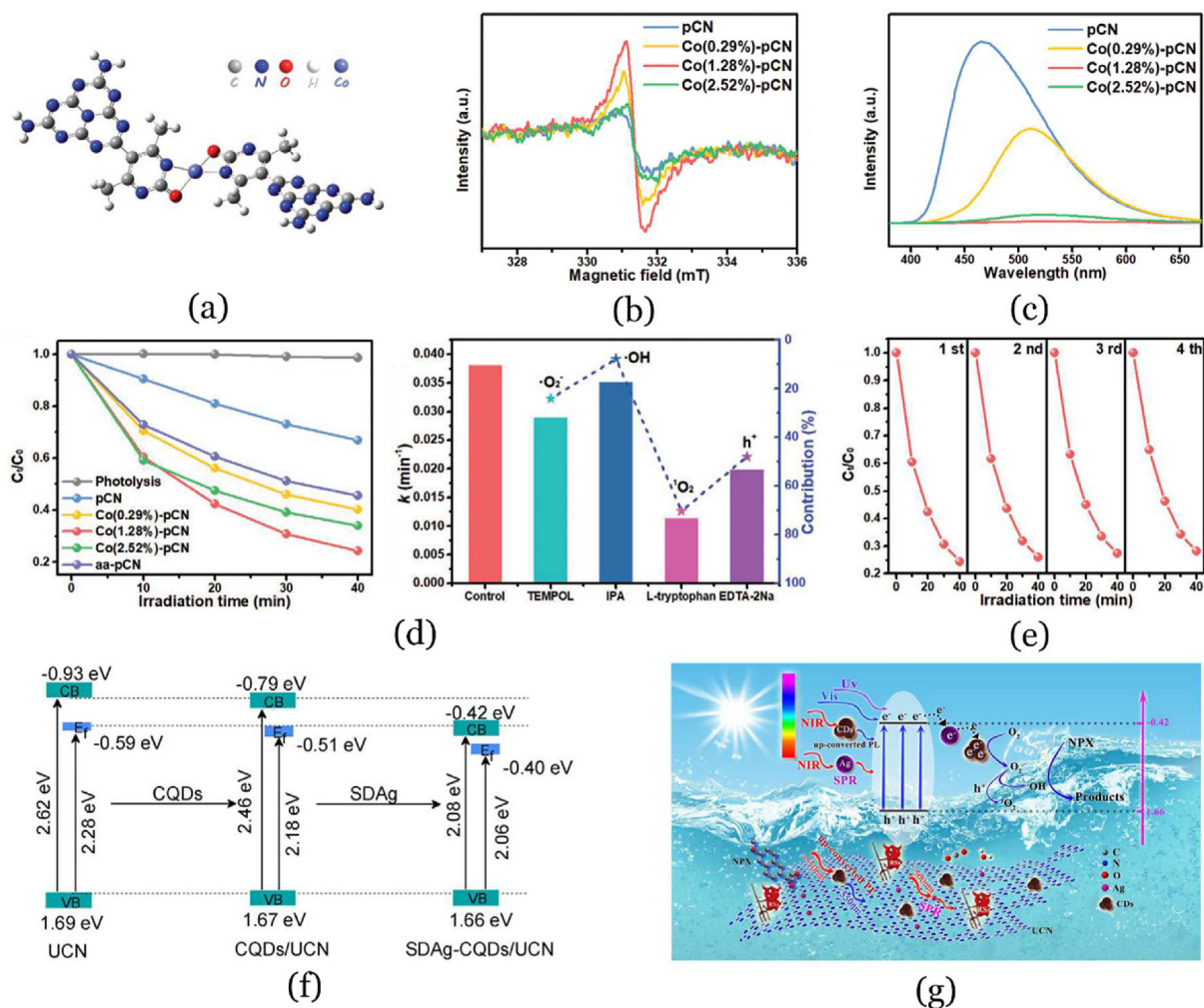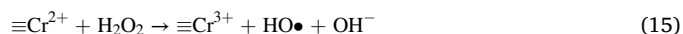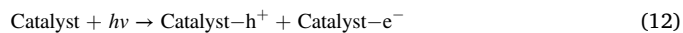For instance, synthesized with a facile pyrolysis process, Wang et al.

Fig. 8. (a) Optimized configuration of Co(1.28%)–pCN. (b) ESR, and (c) PL spectra of different catalysts. (d) Photocatalytic activity toward OTC degradation with various radicals. (e) Stability test of the catalyst [180]. Reproduced with permission: Copyright 2020, Wiley−VCH Verlag GmbH & Co. KGaA, Weinheim. (f) Schematic band structures of UCN, CQDs/UCN, and SDAg−CQDs/UCN. (g) Proposed photocatalytic mechanism for the elimination of NPX [181]. Reproduced with permission: Copyright 2017, Elsevier.

constructed a promising photocatalyst through inserting Fe SAs into the interlayer space between g−C$_3$N$_4$ and rGO layer (C$_3$N$_4$−Fe−rGO), and developed an efficient photo−PDS route for tetracycline (TC) elimination at a wide pH range (0–14) [183]. Protected by the rGO layer, the stability of Fe SAs was significantly enhanced due to the generation of Fe−O structure between Fe and rGO (Fig. 9a). Upon light illumination, the excited electrons primarily localized on g−C$_3$N$_4$ side, while the holes were accumulated on rGO layers, thus facilitating the carrier separation (Fig. 9b). Due to the ingenious design of the sandwich structure, C$_3$N$_4$−Fe−rGO displayed a much−enhanced photocatalytic activity amongst various catalysts using the radicals of HO• and SO$_4^{\bullet-}$ (Fig. 9c). More importantly, acid leaching and agglomeration issues were effectively addressed, and robust active sites enabled the exceptional stability even at strong acidic and alkaline solutions (pH 0–14, Fig. 9d). Impressively, the photo−generated electrons could promote the Fe^{3+} reduction, supplying regenerated Fe^{2+} for on−going PDS activation (Fig. 9e). As discussed previously, promising catalysts with wider pH working ranges are extremely essential for practical applications. This work sheds light on the construction of highly stabilized SACs through the introduction of the double layer confined structures.

Meanwhile, Chen et al. reported a facile and scale−up method for synthesis of single atoms (e.g., Cr, Mn, Fe and Co) anchored flake−like g−C$_3$N$_4$ with plentiful pyrrolic N structures [184]. Taking Cr SAs/g−C$_3$N$_4$ for an example, an impressive catalytic oxidation of BPA

was achieved with a photo−Fenton like procedure. As depicted in Fig. 9f, the unique metalloporphyrin−like CrN$_4$ structure (two pyridinic and two pyrrolic N atoms) enhanced light absorption and trapped photo−induced electrons, improving the separation of charge carriers and providing sufficient reactive sites to boost surface redox reactions (Eq. (12)−14). On one hand, pyrrolic N in the CrN$_4$ offered sufficient electrons to improve the charge density on Cr sites, facilitating the homolytic breakage of peroxide O–O bond to form HO• (Eq. (15)) with higher affinity and lower energy barriers, as confirmed by DFT simulation (Fig. 9g). On the other hand, the photo−generated electrons easily transferred from g−C$_3$N$_4$ substrate to the CrN$_4$ sites, accelerating the redox cycle of Cr^{3+}/Cr^{2+} for continuous H$_2$O$_2$ activation (Eq. (16)). Mimicking the peroxidase for an efficient cleavage of O–O structure, the catalyst with pyrrolic N−rich CrN$_4$ sites enormously enhanced the photocatalytic activity for the pollutant elimination in a wide working pH window (3.0–11.0).

$$\text{Catalyst} + hv \rightarrow \text{Catalyst−h}^+ + \text{Catalyst−e}^- \tag{12}$$

$$\text{O}_2 + \text{e}^- \rightarrow \text{O}_2^{\bullet-} \tag{13}$$

$$\text{OH}^- + \text{h}^+ \rightarrow \text{HO}\bullet \tag{14}$$

$$\equiv\text{Cr}^{2+} + \text{H}_2\text{O}_2 \rightarrow \equiv\text{Cr}^{3+} + \text{HO}\bullet + \text{OH}^- \tag{15}$$

$$\equiv\text{Cr}^{3+} + \text{e}^- \rightarrow \equiv\text{Cr}^{2+} \tag{16}$$
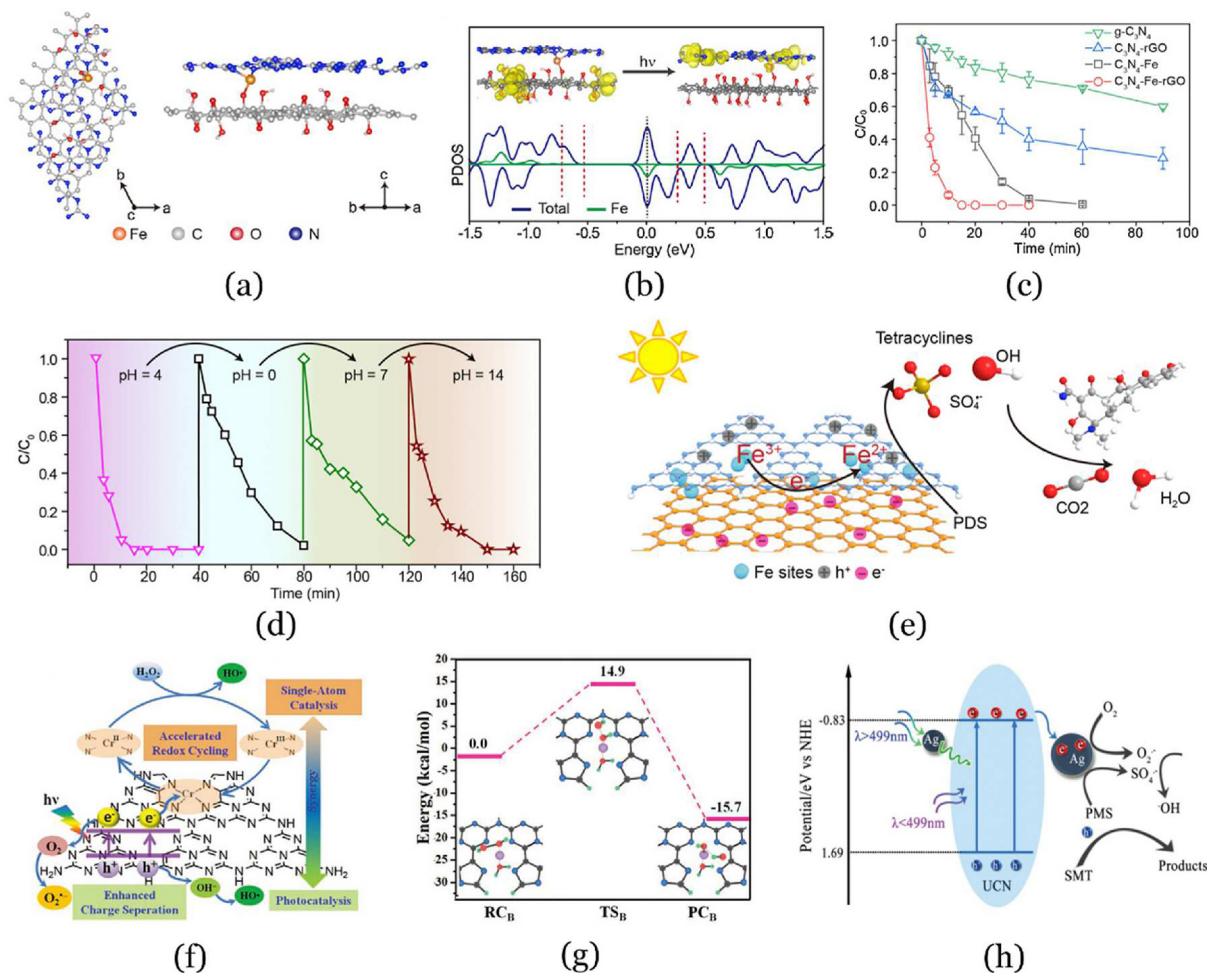
Fig. 9. DFT calculations of (a) the geometrical structure, and (b) carrier dispersion of C_3N_4–Fe−rGO. (c) Degradation performance of TC with various catalysts. (d) The degradation activity with different pH conditions. (e) Proposed reaction route within C_3N_4–Fe−rGO/PDS system [183]. Reproduced with permission: Copyright 2020, Elsevier. (f) Synergistic effect of Cr SAs/g−C_3N_4 in the photo−Fenton system. (g) Free energy profiles for H_2O_2 activation by the CrN_4 sites (two pyridinic and two pyrrolic N atoms) [184]. Reproduced with permission: Copyright 2021, Wiley−VCH GmbH. (h) Schematic illustration of photocatalytic elimination process for SMT within the AgTCM/UCN/PMS system [185]. Reproduced with permission: Copyright 2018, Royal Society of Chemistry.

Comparable with SDAg−CQDs/UCN for the photocatalytic removing of NPX, the incorporation of Ag SAs into UCN also demonstrated an attractive performance in environmental remediation through a pho-to−PMS route [185]. The ultrathin structure of UCN supplied sufficient active centers and shortened the electron migration route, while the anchored Ag SAs improved light absorbance ($\lambda > 499$ nm) and signifi-cantly boosted the electron transfer (Fig. 9h). As a consequence, these photo−induced e^-−h^+ pairs were effectively separated, with the elec-trons rapidly migrated to Ag sites. The accumulated electrons partici-pated in the activation of PMS and interacted with dissolved O_2 to produce $SO_4^{\bullet-}$, $O_2^{\bullet-}$, and HO• as well, significantly boosting the photo-catalytic activity toward sulfamethazine (SMT) decomposition.

Stimulated by these fantastic researches, both suitable single atoms as main active sites, and the controllable regulation of unique coordination structure of these active centers within selected supports, are highly recommended to be taken into consideration for the construction of promising 2D SACs. The synergistic effects (e.g., diverse boosted acti-vation routes, enhanced adsorption toward the pollutants, protection or regeneration of active single atom sites) arising from single atom-−support interactions play crucial roles in the aqueous pollutant elimi-nation, resulting in robust and highly stable catalytic performance. That is the main reason accounts for that supported SACs generally display superior activities to their counterparts of metal ion based homogenous systems.

4.2. Removal of gaseous environmental pollutants

4.2.1. VOC removals

In addition to aqueous pollutants, a variety of gaseous contaminants (e.g., VOCs and NO_x) are extensively discharged from various industrial processes, imposing serious damages to the ecological environment and human health. To this end, different techniques have been developed for the elimination of these gaseous pollutants, such as photocatalytic decomposition, non−thermal plasma oxidation, and thermal catalytic degradation [186–188]. Instead of non−noble metals (e.g., Fe, Cu and Co) widely used in the removing of aqueous pollutants, metal−oxide supported noble metals (e.g., Pt and Ag) are extensively applied to realize an efficient removal of VOCs [189,190]. Compared with carbon−based supports (e.g., graphene and g−C_3N_4), metal oxides (e.g., MnO_x, TiO_2 and CeO_2) not only display excellent stability especially suitable for thermal catalytic procedures, but also possess abundant oxygen va-cancies or active oxygen species on the surface, serving as promising supports for loading active metals to achieve excellent catalytic oxidation of VOCs [191,192]. Attributed to fully−exposed active centers and enhanced interfacial interaction, SACs have demonstrated as promising candidates with high efficiencies toward the elimination of gaseous pollutants. For example, Pt SAs on a mesoporous Fe_2O_3 support (0.25 Pt_1/meso−Fe_2O_3) demonstrated an impressive activity and superior water−resistant ability in thermal decomposition of benzene,

outperforming its counterpart of Pt nanoparticles [131]. Comparably, a similar 0.5 Pt$_1$/Fe$_2$O$_3$ catalyst displayed an effective purification toward toluene, utilizing solar light driven photo−thermal catalytic process [193].

In the purification of VOCs by 2D SACs, enormous efforts have been dedicated to developing promising candidates to achieve high removal efficiency and selectivity. Taking 1,2−dichloroethane (1,2−DCE) with high toxicity and low biodegradability as a target, Lin et al. immobilized Ru SAs on mesoporous γ−Al$_2$O$_3$ (Ru SACs/m−γ−Al$_2$O$_3$) to boost the catalytic performance toward 1,2−DCE degradation to generate CO$_2$ and HCl (Fig. 10a) [194]. The γ−Al$_2$O$_3$ displayed a typical schistose morphology (Fig. 10b), and the isolated Ru SAs were homogeneously stabilized in the support through the formation of Ru$_1$−O$_5$ sites (Fig. 10c). In contrast to Ru nanoparticles/m−γ−Al$_2$O$_3$, Ru SACs/m−γ−Al$_2$O$_3$ with high acidity and less amount of robust redox sites not only facilitated the adsorption of 1,2−DCE, but also promoted a selective dechlorination procedure, following by the decomposition of the products (e.g., the

vinyl alcohol). Accordingly, Ru SACs/m−γ−Al$_2$O$_3$ significantly reduced T$_{50}$ (215 °C) and T$_{90}$ (289 °C) for 1,2−DCE conversion, in contrast to the counterparts of Ru nanoparticles/m−γ−Al$_2$O$_3$ (291 and 374 °C) and m−γ−Al$_2$O$_3$ (323 and 386 °C). Besides the activity and selectivity, the stability is another critical aspect of an eligible catalyst. As expected, robust stability toward a high conversion of 1,2−DCE (~95%) as well as excellent resistance to Cl$_2$ poisoning were acquired with Ru SACs/m−γ−Al$_2$O$_3$ (Fig. 10d).

As one of typical VOCs, toluene possesses a negative impact on human health and environment safety. Developing active catalysts for toluene removal is thus urgently desired. To this end, Zhang et al. successfully immobilized several single atoms (e.g., Y, La and Pt) into structure defects within ultrathin MnO$_2$ nanosheets, and systematically explored their activities for toluene oxidation [196,197]. Taking the La/MnO$_2$ as the paradigm [197], the La doping induced the formation of sufficient surface oxygen species, abundant Mn vacancies, and high specific surface area. Through the activation of surface oxygen species, the resultant
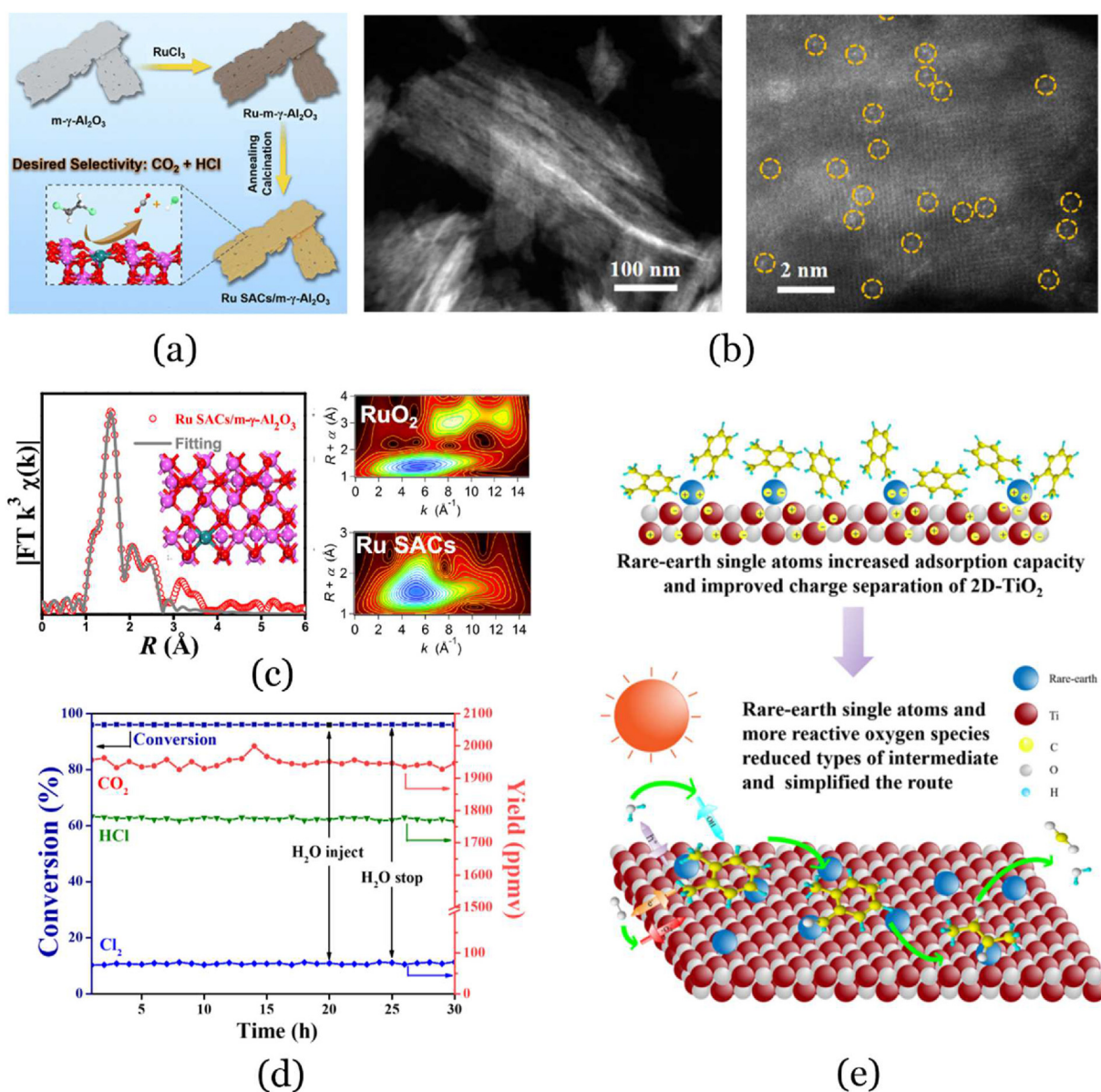

Fig. 10. (a) Selective degradation of 1,2−DCE with Ru SACs/m−γ−Al$_2$O$_3$. (b) TEM and AC−HAADF−STEM images, (c) FT−EXAFS fitting curve and wavelet transform plot of Ru SACs/m−γ−Al$_2$O$_3$. (d) The stability test of Ru SACs/m−γ−Al$_2$O$_3$ [194]. Reproduced with permission: Copyright 2021, American Chemical Society. (e) Schematic diagram of photocatalytic O−xylene degradation on rare−earth single atom−decorated TiO$_2$ [195]. Reproduced with permission: Copyright 2021, Elsevier.

active radicals (e.g., HO•) were responsible for the efficient degradation of toluene into CO_2, somewhat superior to that of Pt SAs on MnO_2.

Recently, Pt SAs located on MgO nanosheets (Pt SAs/MgO) were constructed for an efficient thermal toluene oxidation, based on an enhanced activation process toward the molecular O_2 [130]. The introduction of Pt SAs promoted the generation of oxygen vacancies on MgO, extensively accelerating the adsorption and activation of O_2 for the elimination of VOCs. The adsorbed O_2 was firstly dissociated into *O ($O_2 \rightarrow 2$*O), and the *O further reacted with H_2O (*O + $H_2O \rightarrow 2$HO•) to generate active HO• to participate the catalytic reaction. In contrast to a high activation energy (4.13 eV) within the rate−determining step of O_2 activation on MgO, a significantly reduced energy of 2.48 eV was estimated on Pt SAs/MgO. Accordingly, plentiful active HO• radicals were readily generated on the Pt SAs/MgO, displaying significantly improved catalytic activity compared with the MgO. In contrast to mostly reported researches that the presence of H_2O poisoned the catalysts [198], the dissociation of O_2 on the surface of Pt SAs/MgO to create the HO• was extensively enhanced with the assistance of H_2O, achieving an excellent oxidation of toluene.

In addition to these thermal treatment processes, photocatalysis also provides an attractive route to achieve efficient removals of VOCs. As an attempt, Pt SAs decorated on TiO_2 nanosheets were synthesized for photocatalytic elimination and mineralization of gaseous acetaldehyde [199]. The anchored Pt SAs increased light harvesting, and served as a reservoir to receive the photo−generated electrons from TiO_2, thus tremendously improving the charge separation efficiency for the subsequent generation of active species. Oxidized with the formed HO• and $O_2^{\bullet-}$ radicals, acetaldehyde was eventually converted to CO_2. As an alternative of noble metal, rare−earth Er and La SAs modified TiO_2 nanosheets constructed by a facile impregnation−calcination approach were applied for the elimination of VOCs [195]. Owing to larger metal atom sizes with high coordination numbers, and the orbital hybridization of single atoms with O atoms providing a favorable charge transfer channel, the introduction of Er and La not only extensively enhanced the adsorption capacity toward the pollutant, but also improved the charge separation ability (Fig. 10e). The photo−generated electrons interacted with O_2 to form $O_2^{\bullet-}$, while corresponding holes reacted with H_2O to produce active HO•. Accordingly, Er and La doped TiO_2 displayed significantly boosted photocatalytic degradation activities for O−xylene, superior to pristine TiO_2 nanosheets.

Impressively, great progresses have been achieved in the applications of SACs toward the degradation of VOCs. Particularly, their unique properties could significantly reduce the energy barriers, thus remarkably boosting the elimination efficiency and reducing the operation temperatures. As it is well known, lower catalytic temperature is preferable and prerequisite for practical applications.

4.2.2. NO_x removals

For familiar NO_x (e.g., NO and NO_2), an ideal decomposition of these pollutants into N_2 and O_2 is highly desirable. However, plentiful oxidative agents such as O_2 usually coexisting in the system make the reaction dynamically difficult. Thus, it is requisite for the usage of reductants (e.g., NH_3, CO or H_2) to achieve an efficient conversion into N_2. Recently, SACs have attracted enormous interest in the elimination of NO_x due to their excellent performance. For instance, Zhang et al. demonstrated favorable adsorption and dissociation of NO molecules on Pt SAs anchored FeO_x support (Pt_1/FeO_x) [200]. The sufficient O vacancies within the FeO_x support facilitated NO reduction by its adsorption of dissociated O atoms. Via the reduction in H_2 atmosphere, a high NO conversion and N_2 selectivity were achieved on Pt_1/FeO_x, significantly superior to supported Pt nanoparticles. Alternatively, the selective and deep oxidation of NO_x to NO_x^- on Fe SAs/TiO_2, Ru SA/NH_2−UiO−66−MnO_2 and Pd SAs/TiO_2 provided a new route for efficient NO_x elimination [132,133, 201]. For example, via the interaction between Fe 3d and Ti 3d orbitals, the Fe SAs occupied Ti vacancies and generated the Fe–Ti bond. These dual active Fe and Ti sites of Fe SAs/TiO_2 with modulated electronic

structures facilitated the adsorption and activation of NO and O_2, greatly boosting the NO oxidation to NO_3^- and suppressing the NO_2 generation [132].

In spite of rapid progresses achieved with the NO reduction/oxidation on SACs, related experimental researches focused on 2D SACs are seldom reported. Up to now, several theoretical simulations with the models of Co SAs/N−doped graphene, and Cr SAs/graphyne were established for exploring the NO reduction/oxidation [202,203]. Taking the Cr SAs/-graphyne for example, the overlap of 3d orbitals of Cr atom with the sp hybrid orbital of C atoms, as well as the charge migration from the Cr atom to the graphyne, endowed a robust interaction of Cr SAs on the H1 site of graphyne surface. More importantly, due to the existence of metal 3d orbitals closing to the E_f, the Cr SAs/graphyne with a superior binding capacity toward both NO and O_2 would facilitate the NO reduction (N_2O or N_2 as the products) and oxidation (NO_2 as the product), outperforming its counterparts like Fe, Co and Mn SAs. In the NO oxidation following a kinetically favorable Langmuir−Hinshelwood pathway, the NO and O_2 were firstly co-adsorbed on adjacent Cr sites, generating the peroxide−like (OONO) intermediates. The subsequent cleavage of O–O bond within the OONO resulted in the dissociation of NO_2, leading to the formation of an atomic O on the surface for further reactions.

Inspiringly, these pioneering experimental and theoretical explorations definitely provide supportive guidelines for the design and preparation of promising 2D SACs for NO_x treatments. Notably, in addition to screening proper active single atoms, the selection of suitable supports also greatly contributes to a satisfactory catalytic performance. The resultant synergistic effect would facilitate the adsorption and activation of NO_x, thus remarkably lowering the energy barrier for a highly efficient removal.

4.3. Transformation of environmental pollutants with 2D SACs

In addition to the elimination of environmental contaminants with 2D SACs, alternative transformation routes could not only convert the pollutants into less toxic species, but also produce highly value−added products, opening a new horizon for the pollutant treatment.

4.3.1. Dechlorination of chlorinated phenolics

Chlorinated phenols and phenolic compounds (CPs), as typical harmful disinfection byproducts with acute toxicity, severely threaten the safety of humans and the ecosystem [204]. However, the conventional treatments (e.g., physicochemical and biochemical routes) remain grand challenges, due to an ultrahigh bond energy of C–Cl (~340 kJ mol^{-1}) [205]. To this end, developing efficient dechlorination techniques has attracted ever−growing interest. Performed at ambient conditions with no secondary pollution, the attractive electrocatalytic reduction thus becomes a research hotspot [206]. More importantly, after the dechloriantion treatment, these converted chlorine−free substances could be recycled as industrial raw materials or further eliminated with traditional treatment methods. From the viewpoint of screening proper electrocatalysts, Pd−based candidates have attracted huge interest for an effective dechlorination [207,208]. Pd atoms could promote the Volmer reaction (i.e., $H^+ + e^- \rightarrow$ H*) to create atomic hydrogen (H*), producing reductive species for the replacement of Cl atoms in CPs. In this regard, attractive Pd−based 2D SACs, such as Pd SAs/g−C_3N_4 and Pd SAs/rGO, have been designed and reported recently [209,210].

For example, Niu et al. synthesized Pd SAs loaded rGO (Pd_1/rGO) for electrochemical hydrodechlorination of several chlorophenols [210]. In contrast to common 2D supports, the (3−aminopropyl)−trimethoxylsilane (APTMS) modified rGO possessed an ultra−high specific surface area, abundant surface functionalities, and adequate surface defects for the immobilization of Pd SAs, as well as an excellent electrical conductivity to enable rapid electron transfer for electrocatalytic reactions. Accordingly, negative $PdCl_4^{2-}$ was attracted on the positively charged NH_4^+ groups on the rGO, following by the subsequent photo−reduction to

form Pd$_1$/rGO with the complete removal of residual Cl atoms (Fig. 11a). Instead of the metal−N$_x$ structure, the formed Pd−O sites with unsaturated coordination state not only enhanced the reactant adsorption, but also facilitated electron transfer between Pd and rGO due to the electronic metal−support interactions, leading to a successful hydrodechlorination of 4−CP into phenol. The unique property of Pd SAs effectively restrained the rapid recombination of two H* formed on neighboring Pd atoms (Fig. 11b), resulting in a much higher performance toward 4−CP reduction to its counterpart of Pd nanoparticles (Fig. 11c, ~14 times calculated with the turnover number). Impressively, the electrocatalyst demonstrated an acceptable dechlorination activity for other CPs like 2,4−DCP and 2,4,6−trichlorophenol (2,4,6−TCP) into phenol, providing a general route for the efficient dechlorination treatment.

Despite the superior activities of noble metal−based catalysts (e.g.,

Pd and Ag) in the electrocatalytic dechlorination [211,212], the high cost as well as limited storage severely hindered their wide applications. As an alternative, various noble metal−free catalysts have been developed to achieve rapid dechlorination procedures, such as Cu−Ni bimetallic catalyst, cobalt phosphorous/oxide hybrid and Co/Ni doped MoS$_2$ [213–215]. From the perspective of SACs, Xu et al. constructed atomically dispersed Ni, Fe and Co on N−doped graphene, and systematically investigated the catalytic performance as well as the mechanisms in electrocatalytic dechlorination of chloroacetic acids [216]. Taking stabilized Ni SAs for example (A−Ni−NG), the 2D graphene with crumpled surface facilitated the dispersion of Ni atoms, through the formation of Ni−N bond within the carbon framework. In contrast to pristine N−doped graphene, the introduction of Ni SAs displayed more thermodynamically favorable electron transfer routes. Coupling the appropriate interactions between A−Ni−NG and trichloroacetic acid (TCAA), the A−Ni−NG
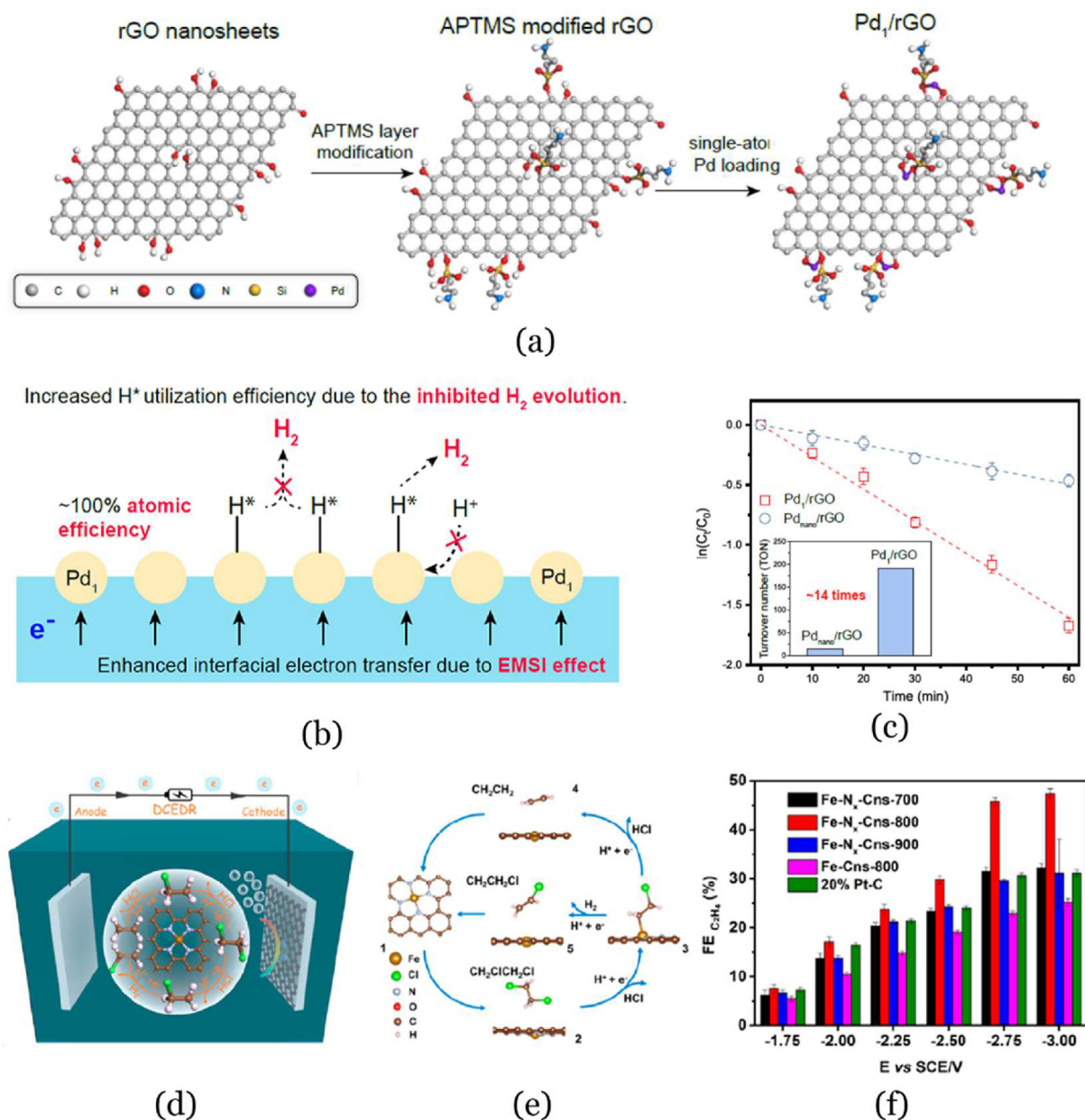

Fig. 11. (a) Schematic synthesis procedure for Pd$_1$/rGO. (b) Suppressed H$_2$ evolution for enhanced hydrodechlorination of 4−CP. (c) Catalytic performance of 4−CP dechlorination with various catalysts [210]. Reproduced with permission: Copyright 2021, American Chemical Society. (d) Electrocatalytic dechlorination of 1,2−DCE. (e) Proposed dechlorination route on the FeN$_4$ site. (f) Faradaic efficiency of different catalysts [16]. Reproduced with permission: Copyright 2020, American Chemical Society.

demonstrated outstanding catalytic dechlorination performance than its counterparts like Ni nanoparticles and Ni foam, following the pathway of TCAA → dichloroacetic acid (DCAA) → monochloroacetic acid (MCAA) → acetic acid (AA).

Moreover, Fe SAs modified carbon nanosheets (Fe−N$_x$−Cns) with highly active FeN$_4$ structure were synthesized for electrocatalytic dechlorination of 1,2−DCE (Fig. 11d) [16]. The produced high−value ethylene is a pivotal raw material for synthesizing plentiful chemicals in industry. Due to the strong electron affinity, 1,2−DCE was quickly adsorbed on Fe sites to generate a *$^-$CH$_2$ClCH$_2$Cl ion after receiving the electrons, following by a decomposition to *$^-$CH$_2$ClCH$_2$ and chloride ions. Interestingly, FeN$_4$ sites were demonstrated to facilitate further dechlorination of *$^-$CH$_2$ClCH$_2$ (*$^-$CH$_2$ClCH$_2$ → *$^-$CH$_2$CH$_2$ + HCl) to produce ethylene (Fig. 11e), while FeN$_3$ centers promoted the dehydrogenation process (*$^-$CH$_2$ClCH$_2$ → *$^-$CHClCH$_2$ + H$_2$) to form vinyl chloride. Due to sufficient FeN$_4$ coordination sites within the Fe−N$_x$−Cns−900, a high activity and ethylene selectivity in 1,2−DCE dechlorination was achieved, superior to that of commercial Pt/C catalyst (Fig. 11f). Inspired by this work, developing 2D SACs with desirable coordination structures of single atoms to achieve adjustable catalytic behaviors is highly anticipated in future.

In nature, the biocatalytic dehalogenation, for example, using the reductive dehalogenases (Rdh) consisted of Co^{2+} center coordinating with tetrapyrrole−derived macrocycle, could effectively induce the heterolytic cleavage toward organic halides, and eventually eliminate halogen through the formation of Co−halogen intermediates [217]. Enlightened by the enzymatic dehalogenation procedure, Chen et al. synthesized Co SAs anchored on carbon doped boron nitride (Co SAs/BCN) to simulate the Rdh, in which Co SAs acted as an enzyme−like active center [129]. The Co SAs/BCN displayed several impressive merits, making it an attractive candidate for the electrocatalytic dechlorination of chloramphenicol (CAP). Firstly, the locally polarized B−N bonds with electron enriched N sites while lacked B sites provided additional electric field for favorable binding of organochlorides (Fig. 12a). Meanwhile, the doping of C atoms into the BN framework significantly reduced the band gap from initial 4.633 to 0.084 eV, resulting in an improved electrical conductivity for electrocatalytic reaction. Moreover, the immobilized Co SAs possessed a higher net charge of 1.11 than that of Co atom (1.03) within Rdh. Thus, the highest occupied molecular orbital (HOMO) of Co SAs approaching to the E$_f$ was beneficial for electron donation (Fig. 12b). Last but not least, after the adsorption of CAP on Co SAs/BCN, an intensive interaction of Cl–Co
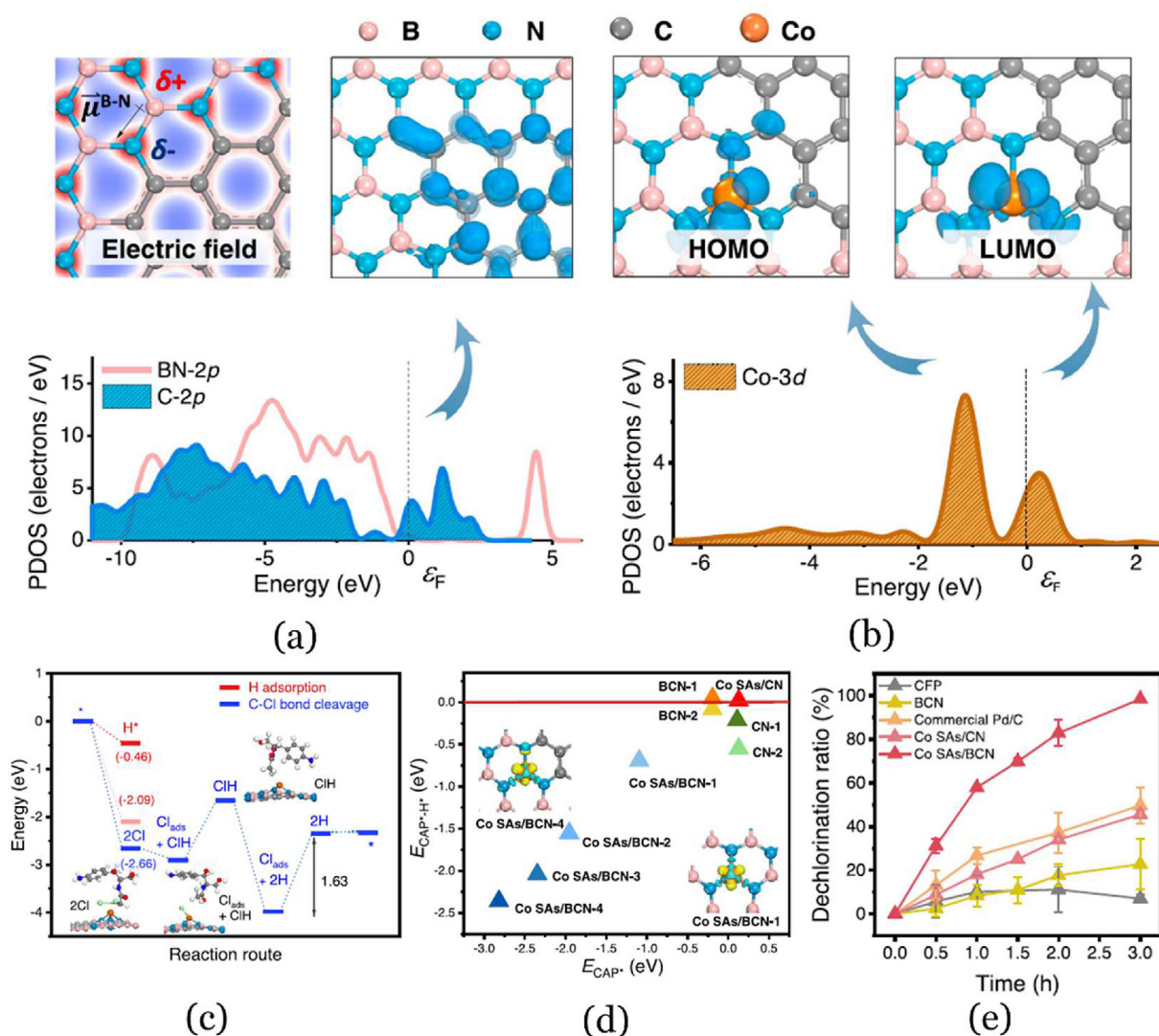

Fig. 12. (a) Electron densities within the BCN, and the corresponding partial density of states (PDOS) plot of BN−2p and C−2p orbitals. (b) HOMO and lowest unoccupied molecular orbital (LUMO) of Co SAs anchored on BCN, and the corresponding PDOS plot of Co−3d orbitals. (c) Energy files of CAP dechlorination on the Co SAs/BCN. (d) Energy difference of E$_{CAP*}$−E$_{H*}$ against the E$_{CAP*}$ for various catalysts. (e) Dechlorination activity toward CAP performed with various catalysts [129]. Reproduced with permission: Copyright 2021, Springer Nature.

bond was formed with the electrons migrated from the Co−3d orbital to the Cl−2p orbital. As another major concern, the H adsorption would not only occupy the catalyst surface, but also suppress CAP adsorption. Impressively, the Co SAs/BCN exhibited a selective adsorption toward CAP* (−2.66 eV) than H* (−0.46 eV), effectively avoided the competitive HER (Fig. 12c). Compared with Co SAs/CN and BCN, a more negative E_{CAP*}−E_{H*} was calculated on the Co SAs/BCN, indicating a higher selectivity toward the reduction of CAP over the HER (Fig. 12d). Attributed to aforementioned merits, the Co SAs/BCN catalyst demonstrated an impressive activity with ~98% dechlorination of CAP, showing significantly boosted performance than those of Co SAs/CN and commercial Pd/C catalyst (Fig. 12e). Inspiringly, this pioneering work would open new horizons for the construction of SACs to mimic the bio−enzymes, greatly promoting their applications for advanced catalysis.

4.3.2. Reduction of nitrophenols

Various kinds of nitrophenols, such as 4−nitrophenol (4−NP), with high water solubility and toxicity, have been listed as priority environmental organic pollutants by the USA−EPA [218]. Notably, as a reduction product of 4−NP, 4−aminophenol (4−AP) not only possesses low toxicity, but also holds great values as an important intermediate product widely used in various fields, such as corrosion inhibition, anti−corrosion lubrication, and drying agent [219]. Therefore, developing promising catalysts toward highly effective conversion from 4−NP to 4−AP is highly desirable, and has attracted enormous attentions in the past few years. Up to now, a variety of catalysts have been reported, mainly including noble metals (e.g., Au, Ag and Pd), non−noble metals (e.g., Cu, Co and Ni), and different carbon materials (e.g., heteroatom doped graphene and porous carbon) [220–226]. In spite of impressive catalytic activities obtained with these noble metal−based catalysts, their further development is severely hindered due to the high cost and limited supplies. The non−noble metals displayed acceptable performance; however, the possible leaching would lead to the decrease in the activity and second pollution. In comparison with metallic catalysts, the carbon materials possess several impressive merits of low cost, bio−degradation, and environmental friendliness. Nevertheless, the observed low conversion efficiencies could not meet the huge requirements for practical applications.

Based on above considerations, the construction of noble metal−based SACs could not only boost the catalytic performance, but also significantly reduce the usage cost due to the maximum atom−utilization efficiency [140,227,228]. Zhang et al. proposed a scalable mass production route for the synthesis of Pd SAs anchored on 2D graphdiyne/graphene heterostructure (Pd$_1$/GDY/G, Fig. 13a) [229]. Utilizing the Eglinton coupling reaction, few−layered GDY was attached on both sides of graphene sheets to produce the GDY/G (Fig. 13b), on account of the lattice match between the GDY and graphene, as well as the van der Waals interaction. Following a wet impregnation reduction strategy, Pd SAs were successfully incorporated into the GDY surface through the
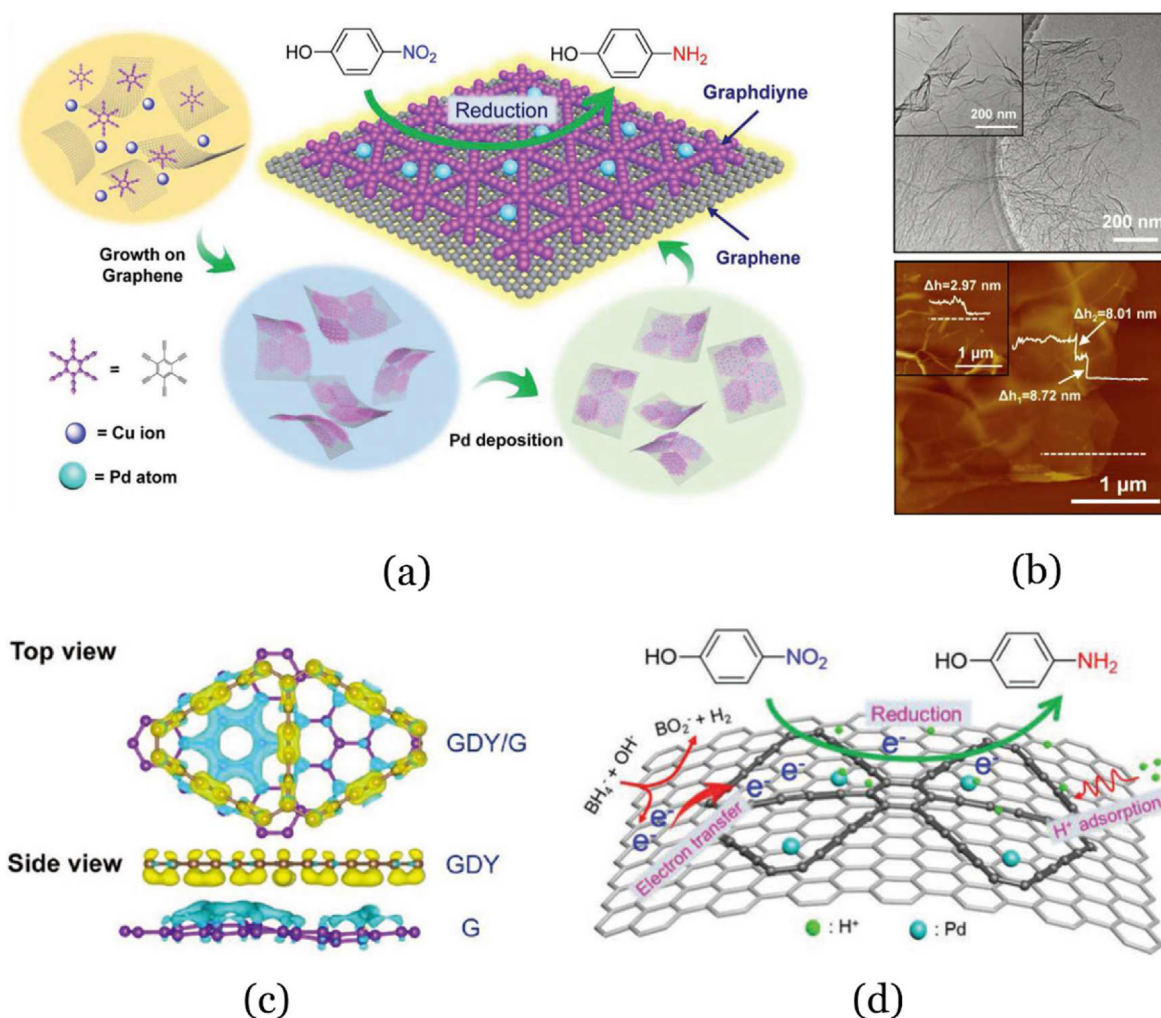

Fig. 13. (a) Schematic route for the construction of Pd$_1$/GDY/G. (b) TEM and AFM images of GDY/G. (c) Electron redistribution within GDY/G. (d) Proposed reaction mechanism in 4−NP reduction with Pd$_1$/GDY/G [229]. Reproduced with permission: Copyright 2019, Wiley−VCH Verlag GmbH & Co. KGaA, Weinheim.

generation of Pd–C/O structure. The introduction of graphene accelerated the electron migration from graphene to GDY, resulting in the charge density redistribution with electrons depleted on graphene (blue regions) while accumulated on the GDY (yellow regions) (Fig. 13c). The accumulated electrons increased the E_f of GDY, as well as the energy of free electron (~0.58 eV), significantly promoting the rate−determining step in the first hydrogenation of the nitro group (adsorbed 4−NP denoted as Ar−NO$_2$*, Ar−NO$_2$* + H$^+$ + e$^-$ → Ar−NOOH*). Utilizing the sufficient H$^+$ in solution and accumulated electrons from the support, Pd$_1$/GDY/G demonstrated an impressive performance toward 4−NP reduction on Pd sites, outperforming to its counterpart of Pd$_1$/GDY (Fig. 13d).

5. Conclusions and perspectives

As an emerging research frontier in heterogeneous catalysis, 2D SACs with uniform geometric structure and unique electronic properties display huge potentials in various catalytic applications. Recently, ever−growing interest has been focused on the environmental remediation with diverse 2D SACs, displaying impressive and superior performance than their nanoparticle counterparts. In this review, various synthesis strategies, advanced characterization tools, as well as the recent progress of 2D SACs for the pollutant elimination and transformation are systematically summarized. The enhanced catalytic activities are mainly ascribed to several aspects. (i) The highly dispersed single atoms realize an efficient atomic utilization due to the full exposure of active sites. (ii) The desirable 2D supports with thin−layer structures provide a high specific area and enhance the availability of single atoms. (iii) The unique metal−support interactions within 2D SACs synergistically boost the catalytic activities. Although satisfactory results have been observed, the present research on 2D SACs for environmental remediation is still in its infancy, particularly compared with the wider applications of 3D SACs, and several challenges are remained to be addressed for further development to achieve ultimate large−scale applications.

(1) Developing and screening suitable and promising 2D supports

For the environmental applications, mostly adopted 2D supports discussed in this review are mainly carbon materials (e.g., graphene and g−C$_3$N$_4$) and metal oxides (e.g., TiO$_2$ and MgO). In spite of attractive merits of these supports, there still exist several issues. For example, the possible destruction of carbon framework by the formed active radicals would lead to the deactivation and reduce stability of constructed catalysts. While for the metal oxide supports, the precise regulation toward ultra−thin structures to achieve the controllable layers is generally difficult. As it is well known, the electronic structure of 2D supports is highly related to the layer numbers, which significantly contribute to final catalytic properties.

For other types of 2D supports, such as MXenes and LDHs with multiple compositions, related SACs are seldom reported for the environmental applications. Inspired by the impressive degradation performance of 2D Co SAs/Ti$_{2-x}$N due to an efficient activation toward PMS [165], it is highly desired for the construction of more promising MXene−based 2D SACs to realize highly−efficient environmental remediation. Moreover, emerging 2D materials like boron nitride (BN) and black phosphorus (BP) also hold great potentials for the construction of 2D SACs [62,108,230]. The BP possesses excellent physical and chemical properties and has a layer−dependent bandgap structure, displaying excellent photothermal and photochemical capability [231–233]. Thus, the combination of single atoms and 2D BP would open a new horizon for the construction of advanced photocatalysts.

To this end, developing and screening proper 2D materials are worthy of further exploration for the construction of efficient 2D SACs, and there exists a huge space to explore their potentials for the environmental applications.

(2) Controllable and scale−up synthesis of high−quality 2D SACs

A high−mass metal loading in SACs is pivotal for practical catalytic reactions, considering that an increased population of single atoms could extensively boost the performance. In mostly reported literatures (shown in Table 1), the metal loading amounts in SACs are generally less than 5 wt%. To achieve this aim, future efforts can be focused on several aspects. From the perspective of supports, the suitable supports with sufficient and homogenously dispersed binding sites are prerequisite for the high−loading and stable immobilization of single atoms. Meanwhile, the accurate regulation toward synthesis conditions and the deeper investigations into the formation mechanisms are also indispensable, since the high−mass loading of metal species generally leads to the easy aggregation because of the high surface energy.

Moreover, the precise manipulation of coordination environment of the single atoms on 2D supports would provide an efficient route for the regulation of the catalytic activity for a desirable application. For example, various coordination structures of FeN$_x$ (e.g., FeN$_3$, FeN$_4$, FeN$_5$ and FeN$_6$) displayed distinct electrocatalytic behaviors. It was reported that FeN$_3$ and FeN$_4$ sites were preferable for NRR, FeN$_5$ served as the main active site for CRR, while FeN$_6$ structure was estimated as real active center for ORR [66,234–236]. Meanwhile, for a deeper understanding toward active sites, it is stringent to adopt more sensitive atomic−resolution imaging techniques (e.g., STM) to directly characterize these coordination structures.

Besides the controllable preparation of 2D SACs, exploring and developing a scalable approach for the mass production of SACs is the prerequisite for the wide applications. The current techniques for the synthesis of SACs generally suffer from different limitations. For instance, ALD or CVD route requires the sophisticated instruments, and the stability of the resultant catalysts under harsh condition should be improved in future. While for the pyrolysis route with a scalable production, a precise control of the position and amounts of active sites is not easy.

Thus, developing facile and controllable approaches for the construction of high−quality 2D SACs is urgent and anticipated to meet the demands for a scalable and industrial level of production.

(3) In−depth investigations into reaction mechanisms with designed 2D SACs

The profound explorations toward the reaction pathways, along with the monitoring of variations in the surface property and texture of constructed catalysts, are of critical importance for revealing the underlying mechanisms. At present, great challenges are still remained in 2D SACs for the environmental remediation. For example, within the non−radical routes that excluding the case of ^{1}O$_2$, an in−depth study toward the claimed electron transfer route and in−situ monitoring with high sensitivity for reaction intermediates are highly expected to provide more direct and accurate evidences. To this end, operando characterization techniques, such as in−situ XRD, XAS, XPS, and FTIR analysis, are urgently required. Through the timely acquisition of the property changes on the surface of 2D SACs, the straightforward and convincing information, such as the evolutions of metastable intermediates and even dynamic charge transfer, would be obtained.

Moreover, the theoretical investigation is a robust tool to probe the catalytic nature of 2D SACs at the atomic levels. Particularly, the relatively uniform structures make the 2D supports proper candidates for the fundamental explorations toward the reaction processes through theoretical calculations. In this regard, developing advanced theoretical calculation methods with high throughput screenings are desirable, taking critical factors that significantly contribute to catalytic behaviors into considerations.

Coupling the evidences obtained from in−situ characterizations and theoretical simulations, the solid understanding toward the underlying catalytic mechanisms could be effectively realized, offering an efficient guidance for designing attractive 2D SACs for the desired applications.

(4) 2D SACs based membrane processes for environmental remediation

Apart from above challenges, another issue is the practical applications of 2D SACs, realizing the highly−efficient and continuous treatments of different environmental pollutants at large scales. Actually, the heterogeneous catalysis with 2D SACs performed through a batch mode in aqueous solutions has several limitations. For example, the separation and recycle of the spent catalysts usually require additional treatment and cost. Recently, 2D materials with unique merits are widely applied as the promising matrix for the construction of functional membranes, achieving attractive performance for the separation and purification [237]. To this end, utilizing the advanced membrane technology and process [238–240], the construction of multifunctional membranes with 2D SACs, and further integration into the membrane reactors are considered as promising development aspects. Through the combination of 2D SACs and membrane processes, a continuous treatment with unlimited potential toward the degradation of various pollutants, as well as the separation of large particles within the industrial wastewater could be achieved.

(5) Extended application of 2D SACs in the treatment of other emerging pollutants

In addition to the above−mentioned considerations, the potential applications of 2D SACs toward efficient treatments of other refractory contaminants, such as microplastics, have received few attentions. As an emerging contaminant, microplastics with a general diameter <5 mm have posed huge threats to marine and terrestrial systems, due to their enormous demand, improper disposal and extreme chemical stability [241,242]. Up to now, enormous efforts have been dedicated to developing efficient remediation strategies. The biodegradation is regarded as an attractive route for microplastics treatment, owing to its low cost and environmental friendliness. Nevertheless, this process is time−consuming and unable of degrading refractory pollutants completely. Alternatively, AOPs−based routes (e.g., photocatalytic, Fenton and Fenton−like systems), although generally conducted with harsh conditions (high temperature or strong acid/alkaline solution), have demonstrated acceptable performance in deformation and remediation of microplastics [243–245]. Enlightened by the discovery that SACs could significantly lower the energy barrier to reduce the operation temperature for catalytic reactions (e.g., the elimination of VOCs), it is highly anticipated that the 2D SACs with exceptional properties would open new horizon for the remediation of these emerging pollutants under mild conditions.

Despite tremendous progress achieved recently, there still remains a long way for the exploration of the controllable and scale−up synthesis of more capable 2D SACs, development of advanced in−situ characterization tools and efficient theoretical simulations, and the integration with membrane technology, to promote the wide applications of 2D SACs in environmental protection and remediation.

Declaration of competing interest

The authors declare that they have no conflict of interest.

Acknowledgements

References

[1] B. Hennig, L. Ormsbee, C.J. McClain, B.A. Watkins, B. Blumberg, L.G. Bachas, W. Sanderson, C. Thompson, W.A. Suk, Environ. Health Perspect. 120 (2012) 771–774.
[2] P. Gaudriault, S. Mazaud-Guittot, V. Lavoue, I. Coiffec, L. Lesne, N. Dejucq-Rainsford, M. Scholze, A. Kortenkamp, B. Jegou, Environ. Health Perspect. 125 (2017), 087004.
[3] G.-L. Yang, X.-L. Jiang, H. Xu, B. Zhao, Small 17 (2021), 2005327.
[4] S.V. Krupa, A.H. Legge, Environ. Pollut. 107 (2000) 31–45.
[5] S.L. Liu, D. Krewski, Y.L. Shi, Y. Chen, R.T. Burnett, Environ. Health Perspect. 111 (2003) 1773–1778.
[6] M. Phillips, K. Gleeson, J.M. Hughes, J. Greenberg, R.N. Cataneo, L. Baker, W.P. McVay, Lancet 353 (1999) 1930–1933.
[7] B. Huang, C. Lei, C. Wei, G. Zeng, Environ. Int. 71 (2014) 118–138.
[8] S. Wang, H. Sun, H.M. Ang, M.O. Tade, Chem. Eng. J. 226 (2013) 336–347.
[9] Y. Boyjoo, H. Sun, J. Liu, V.K. Pareek, S. Wang, Chem. Eng. J. 310 (2017) 537–559.
[10] P. Kar, K. Shukla, P. Jain, G. Sathiyan, R.K. Gupta, Nano Mater. Sci. 3 (2021) 25–46.
[11] B.O. Okesola, D.K. Smith, Chem. Soc. Rev. 45 (2016) 4226–4251.
[12] X. Duan, H. Sun, S. Wang, Acc. Chem. Res. 51 (2018) 678–687.
[13] Y. Yin, W. Li, C. Xu, L. Shi, L.-C. Zhang, Z. Ao, M. Liu, M. Lu, X. Duan, S. Wang, S. Liu, H. Sun, Environ. Sci.: Nano 7 (2020) 2595–2606.
[14] C. He, J. Cheng, X. Zhang, M. Douthwaite, S. Pattisson, Z. Hao, Chem. Rev. 119 (2019) 4471–4568.
[15] G. Liao, Y. Gong, L. Zhong, J. Fang, L. Zhang, Z. Xu, H. Gao, B. Fang, Nano Res. 12 (2019) 2407–2436.
[16] G. Gan, X. Li, L. Wang, S. Fan, J. Mu, P. Wang, G. Chen, ACS Nano 14 (2020) 9929–9937.
[17] M. Abbas, M.A.Z.G. Sial, Nano Mater. Sci. 3 (2021) 368–389.
[18] X.-F. Yang, A. Wang, B. Qiao, J. Li, J. Liu, T. Zhang, Acc. Chem. Res. 46 (2013) 1740–1748.
[19] B. Qiao, A. Wang, X. Yang, L.F. Allard, Z. Jiang, Y. Cui, J. Liu, J. Li, T. Zhang, Nat. Chem. 3 (2011) 634–641.
[20] P. Yin, T. Yao, Y. Wu, L. Zheng, Y. Lin, W. Liu, H. Ju, J. Zhu, X. Hong, Z. Deng, G. Zhou, S. Wei, Y. Li, Angew. Chem. Int. Ed. 55 (2016) 10800–10805.
[21] J. Jones, H. Xiong, A.T. DeLaRiva, E.J. Peterson, P. Hien, S.R. Challa, G. Qi, S. Oh, M.H. Wiebenga, X.I.P. Hernandez, Y. Wang, A.K. Datye, Science 353 (2016) 150–154.
[22] H. Fei, J. Dong, M.J. Arellano-Jimenez, G. Ye, N.D. Kim, E.L.G. Samuel, Z. Peng, Z. Zhu, F. Qin, J. Bao, M.J. Yacaman, P.M. Ajayan, D. Chen, J.M. Tour, Nat. Commun. 6 (2015) 8668.
[23] J. Deng, H. Li, J. Xiao, Y. Tu, D. Deng, H. Yang, H. Tian, J. Li, P. Ren, X. Bao, Energy Environ. Sci. 8 (2015) 1594–1601.
[24] P. Ares, K.S. Novoselov, Nano Mater. Sci. 4 (2022) 3–9.
[25] Q. Wang, D. O'Hare, Chem. Rev. 112 (2012) 4124–4155.
[26] C. Huang, Y. Li, N. Wang, Y. Xue, Z. Zuo, H. Liu, Y. Li, Chem. Rev. 118 (2018) 7744–7803.
[27] J. Zhu, E. Ha, G. Zhao, Y. Zhou, D. Huang, G. Yue, L. Hu, N. Sun, Y. Wang, L.Y.S. Lee, C. Xu, K.-Y. Wong, D. Astruc, P. Zhao, Coord. Chem. Rev. 352 (2017) 306–327.
[28] F. Wang, M. Hao, W. Liu, P. Yan, B. Fang, S. Li, J. Liang, M. Zhu, L. Cui, Nano Mater. Sci. 3 (2021) 205–212.
[29] Z. Liu, Z. Zhao, Y. Wang, S. Dou, D. Yan, D. Liu, Z. Xia, S. Wang, Adv. Mater. 29 (2017), 1606207.
[30] B. Dai, K. Chen, Y. Wang, L. Kang, M. Zhu, ACS Catal. 5 (2015) 2541–2547.
[31] J. Long, X. Xie, J. Xu, Q. Gu, L. Chen, X. Wang, ACS Catal. 2 (2012) 622–631.
[32] A. Alarawi, V. Ramalingam, J.-H. He, Mater. Today Energy 11 (2019) 1–23.
[33] R. Gusmao, M. Vesely, Z. Sofer, ACS Catal. 10 (2020) 9634–9648.
[34] W.-J. Niu, J.-Z. He, B.-N. Gu, M.-C. Liu, Y.-L. Chueh, Adv. Funct. Mater. 31 (2021), 2103558.
[35] A.B. Yankovich, B. Berkels, W. Dahmen, P. Binev, S.I. Sanchez, S.A. Bradley, A. Li, I. Szlufarska, P.M. Voyles, Nat. Commun. 5 (2014) 4155.
[36] Y. Shang, X. Xu, B. Gao, S. Wang, X. Duan, Chem. Soc. Rev. 50 (2021) 5281–5322.
[37] J. Yang, W. Li, D. Wang, Y. Li, Adv. Mater. 32 (2020) 2003300.
[38] C. Gao, J. Low, R. Long, T. Kong, J. Zhu, Y. Xiong, Chem. Rev. 120 (2020) 12175–12216.
[39] B. Zhang, T. Fan, N. Xie, G. Nie, H. Zhang, Adv. Sci. 6 (2019), 1901787.
[40] Y. Wang, J. Mao, X. Meng, L. Yu, D. Deng, X. Bao, Chem. Rev. 119 (2019) 1806–1854.
[41] P. Wang, D. Zhao, L. Yin, Energy Environ. Sci. 14 (2021) 1794–1834.
[42] X.-P. Yin, H.-J. Wang, S.-F. Tang, X.-L. Lu, M. Shu, R. Si, T.-B. Lu, Angew. Chem. Int. Ed. 57 (2018) 9382–9386.
[43] Y. Xue, B. Huang, Y. Yi, Y. Guo, Z. Zuo, Y. Li, Z. Jia, H. Liu, Y. Li, Nat. Commun. 9 (2018) 1460.
[44] A.W. Robertson, Y.-C. Lin, S. Wang, H. Sawada, C.S. Allen, Q. Chen, S. Lee, G.-D. Lee, J. Lee, S. Han, E. Yoon, A.I. Kirkland, H. Kim, K. Suenaga, J.H. Warner, ACS Nano 10 (2016) 10227–10236.
[45] A. Han, X. Zhou, X. Wang, S. Liu, Q. Xiong, Q. Zhang, L. Gu, Z. Zhuang, W. Zhang, F. Li, D. Wang, L.-J. Li, Y. Li, Nat. Commun. 12 (2021) 709.
[46] Z. Cai, B. Liu, X. Zou, H.-M. Cheng, Chem. Rev. 118 (2018) 6091–6133.
[47] J. Zhou, J. Lin, H. Sims, C. Jiang, C. Cong, J.A. Brehm, Z. Zhang, L. Niu, Y. Chen, Y. Zhou, Y. Wang, F. Liu, C. Zhu, T. Yu, K. Suenaga, R. Mishra, S.T. Pantelides, Z.-G. Zhu, W. Gao, Z. Liu, W. Zhou, Adv. Mater. 32 (2020), 1906536.
[48] L. Zhang, M.N. Banis, X. Sun, Natl. Sci. Rev. 5 (2018) 628–630.

[49] H. Yan, X. Zhao, N. Guo, Z. Lyu, Y. Du, S. Xi, R. Guo, C. Chen, Z. Chen, W. Liu, C. Yao, J. Li, S.J. Pennycook, W. Chen, C. Su, C. Zhang, J. Lu, Nat. Commun. 9 (2018) 3197.

[50] S. Sun, G. Zhang, N. Gauquelin, N. Chen, J. Zhou, S. Yang, W. Chen, X. Meng, D. Geng, M.N. Banis, R. Li, S. Ye, S. Knights, G.A. Botton, T.-K. Sham, X. Sun, Sci. Rep. 3 (2013) 1775.

[51] H. Yan, H. Cheng, H. Yi, Y. Lin, T. Yao, C. Wang, J. Li, S. Wei, J. Lu, J. Am. Chem. Soc. 137 (2015) 10484–10487.

[52] Y. Qu, Z. Li, W. Chen, Y. Lin, T. Yuan, Z. Yang, C. Zhao, J. Wang, C. Zhao, X. Wang, F. Zhou, Z. Zhuang, Y. Wu, Y. Li, Nat. Catal. 1 (2018) 781–786.

[53] Y. Qu, B. Chen, Z. Li, X. Duan, L. Wang, Y. Lin, T. Yuan, F. Zhou, Y. Hu, Z. Yang, C. Zhao, J. Wang, C. Zhao, Y. Hu, G. Wu, Q. Zhang, Q. Xu, B. Liu, P. Gao, R. You, W. Huang, L. Zheng, L. Gu, Y. Wu, Y. Li, J. Am. Chem. Soc. 141 (2019) 4505–4509.

[54] L. Lin, Z. Chen, W. Chen, Nano Res. 14 (2021) 4398–4416.

[55] Z. Luo, Y. Ouyang, H. Zhang, M. Xiao, J. Ge, Z. Jiang, J. Wang, D. Tang, X. Cao, C. Liu, W. Xing, Nat. Commun. 9 (2018) 2120.

[56] D. Zhao, Z. Chen, W. Yang, S. Liu, X. Zhang, Y. Yu, W.-C. Cheong, L. Zheng, F. Ren, G. Ying, X. Cao, D. Wang, Q. Peng, G. Wang, C. Chen, J. Am. Chem. Soc. 141 (2019) 4086–4093.

[57] W. Bi, X. Li, R. You, M. Chen, R. Yuan, W. Huang, X. Wu, W. Chu, C. Wu, Y. Xie, Adv. Mater. 30 (2018), 1706617.

[58] G. Vilé, D. Albani, M. Nachtegaal, Z. Chen, D. Dontsova, M. Antonietti, N. López, J. Pérez-Ramírez, Angew. Chem. Int. Ed. 54 (2015) 11265–11269.

[59] Y. Gao, Z. Cai, X. Wu, Z. Lv, P. Wu, C. Cai, ACS Catal. 8 (2018) 10364–10374.

[60] B. Anasori, M.R. Lukatskaya, Y. Gogotsi, Nat. Rev. Mater. 2 (2017), 16098.

[61] K. Jiang, S. Siahrostami, T. Zheng, Y. Hu, S. Hwang, E. Stavitski, Y. Peng, J. Dynes, M. Gangisetty, D. Su, K. Attenkofer, H. Wang, Energy Environ. Sci. 11 (2018) 893–903.

[62] S. Zhao, G. Chen, G. Zhou, L.-C. Yin, J.-P. Veder, B. Johannessen, M. Saunders, S.-Z. Yang, R. De Marco, C. Liu, S.P. Jiang, Adv. Funct. Mater. 30 (2020), 1906157.

[63] J.-H. Zhang, W. Yang, M. Zhang, H.-J. Wang, R. Si, D.-C. Zhong, T.-B. Lu, Nano Energy 80 (2021), 105542.

[64] D. Liu, C. Wu, S. Chen, S. Ding, Y. Xie, C. Wang, T. Wang, Y.A. Haleem, Z. ur Rehman, Y. Sang, Q. Liu, X. Zheng, Y. Wang, B. Ge, H. Xu, L. Song, Nano Res. 11 (2018) 2217–2228.

[65] L. Zhao, Y. Zhang, L.-B. Huang, X.-Z. Liu, Q.-H. Zhang, C. He, Z.-Y. Wu, L.-J. Zhang, J. Wu, W. Yang, L. Gu, J.-S. Hu, L.-J. Wan, Nat. Commun. 10 (2019) 1278.

[66] H. Zhang, J. Li, S. Xi, Y. Du, X. Hai, J. Wang, H. Xu, G. Wu, J. Zhang, J. Lu, J. Wang, Angew. Chem. Int. Ed. 58 (2019) 14871–14876.

[67] W. Zang, A. Sumboja, Y. Ma, H. Zhang, Y. Wu, S. Wu, H. Wu, Z. Liu, C. Guan, J. Wang, S.J. Pennycook, ACS Catal. 8 (2018) 8961–8969.

[68] M. Ding, R.W. Flaig, H.-L. Jiang, O.M. Yaghi, Chem. Soc. Rev. 48 (2019) 2783–2828.

[69] S.J. Yang, T. Kim, J.H. Im, Y.S. Kim, K. Lee, H. Jung, C.R. Park, Chem. Mater. 24 (2012) 464–470.

[70] D. Sheberla, J.C. Bachman, J.S. Elias, C.-J. Sun, Y. Shao-Horn, M. Dinca, Nat. Mater. 16 (2017) 220–224.

[71] Y. Yin, Z. Wen, L. Shi, Z. Zhang, Z. Yang, C. Xu, H. Sun, S. Wang, A. Yuan, ACS Sustainable Chem. Eng. 7 (2019) 11284–11292.

[72] T. Zhang, W. Lin, Chem. Soc. Rev. 43 (2014) 5982–5993.

[73] K. Shen, X. Chen, J. Chen, Y. Li, ACS Catal. 6 (2016) 5887–5903.

[74] E. Zhang, T. Wang, K. Yu, J. Liu, W. Chen, A. Li, H. Rong, R. Lin, S. Ji, X. Zhene, Y. Wang, L. Zheng, C. Chen, D. Wang, J. Zhang, Y. Li, J. Am. Chem. Soc. 141 (2019) 16569–16573.

[75] Z. Song, L. Zhang, K. Doyle-Davis, X. Fu, J.-L. Luo, X. Sun, Adv. Energy Mater. 10 (2020), 2001561.

[76] Y.-N. Gong, L. Jiao, Y. Qian, C.-Y. Pan, L. Zheng, X. Cai, B. Liu, S.-H. Yu, H.-L. Jiang, Angew. Chem. Int. Ed. 59 (2020) 2705–2709.

[77] F. Lu, K. Fan, L. Cui, Y. Wang, W. Wang, G. Zhang, C. Wang, Q. Zhang, B. Li, L. Zong, L. Wang, Chem. Eng. J. 431 (2022), 133242.

[78] L. Zheng, S. Yu, X. Lu, W. Fan, B. Chi, Y. Ye, X. Shi, J. Zeng, X. Li, S. Liao, ACS Appl. Mater. Interfaces 12 (2020) 13878–13887.

[79] W. Liu, Y. Chen, H. Qi, L. Zhang, W. Yan, X. Liu, X. Yang, S. Miao, W. Wang, C. Liu, A. Wang, J. Li, T. Zhang, Angew. Chem. Int. Ed. 57 (2018) 7071–7075.

[80] Y. Li, Z.-S. Wu, P. Lu, X. Wang, W. Liu, Z. Liu, J. Ma, W. Ren, Z. Jiang, X. Bao, Adv. Sci. 7 (2020), 1903089.

[81] X. Zhang, S. Zhang, Y. Yang, L. Wang, Z. Mu, H. Zhu, X. Zhu, H. Xing, H. Xia, B. Huang, J. Li, S. Guo, E. Wang, Adv. Mater. 32 (2020), 1906905.

[82] J. Zhang, Y. Zhao, X. Guo, C. Chen, C.-L. Dong, R.-S. Liu, C.-P. Han, Y. Li, Y. Gogotsi, G. Wang, Nat. Catal. 1 (2018) 985–992.

[83] Z. Zhang, C. Feng, C. Liu, M. Zuo, L. Qin, X. Yan, Y. Xing, H. Li, R. Si, S. Zhou, J. Zeng, Nat. Commun. 11 (2020) 1215.

[84] H. Wei, K. Huang, D. Wang, R. Zhang, B. Ge, J. Ma, B. Wen, S. Zhang, Q. Li, M. Lei, C. Zhang, J. Irawan, L.-M. Liu, H. Wu, Nat. Commun. 8 (2017) 1490.

[85] P. Liu, Y. Zhao, R. Qin, S. Mo, G. Chen, L. Gu, M. Chevrier Daniel, P. Zhang, Q. Guo, D. Zang, B. Wu, G. Fu, N. Zheng, Science 352 (2016) 797–800.

[86] S. Yang, Y. Yu, M. Dou, Z. Zhang, L. Dai, F. Wang, Angew. Chem. Int. Ed. 58 (2019) 14724–14730.

[87] X. Cui, H. Li, Y. Wang, Y. Hu, L. Hua, H. Li, X. Han, Q. Liu, F. Yang, L. He, X. Chen, Q. Li, J. Xiao, D. Deng, X. Bao, Chem 4 (2018) 1902–1910.

[88] Y. Zhu, W. Sun, J. Luo, W. Chen, T. Cao, L. Zheng, J. Dong, J. Zhang, M. Zhang, Y. Han, C. Chen, Q. Peng, D. Wang, Y. Li, Nat. Commun. 9 (2018) 3861.

[89] D. Deng, X. Chen, L. Yu, X. Wu, Q. Liu, Y. Liu, H. Yang, H. Tian, Y. Hu, P. Du, R. Si, J. Wang, X. Cui, H. Li, J. Xiao, T. Xu, J. Deng, F. Yang, N. Duchesne Paul, P. Zhang, J. Zhou, L. Sun, J. Li, X. Pan, X. Bao, Sci. Adv. 1 (2015), e1500462.

[90] K. Qi, X. Cui, L. Gu, S. Yu, X. Fan, M. Luo, S. Xu, N. Li, L. Zheng, Q. Zhang, J. Ma, Y. Gong, F. Lv, K. Wang, H. Huang, W. Zhang, S. Guo, W. Zheng, P. Liu, Nat. Commun. 10 (2019) 5231.

[91] H. Fei, J. Dong, Y. Feng, C.S. Allen, C. Wan, B. Volosskiy, M. Li, Z. Zhao, Y. Wang, H. Sun, P. An, W. Chen, Z. Guo, C. Lee, D. Chen, I. Shakir, M. Liu, T. Hu, Y. Li, A.I. Kirkland, X. Duan, Y. Huang, Nat. Catal. 1 (2018) 63–72.

[92] K. Fan, Z. Li, Y. Song, W. Xie, M. Shao, M. Wei, Adv. Funct. Mater. 31 (2021), 2008064.

[93] J. Zhang, J. Liu, L. Xi, Y. Yu, N. Chen, S. Sun, W. Wang, K.M. Lange, B. Zhang, J. Am. Chem. Soc. 140 (2018) 3876–3879.

[94] A.J. Therrien, A.J.R. Hensley, M.D. Marcinkowski, R. Zhang, F.R. Lucci, B. Coughlin, A.C. Schilling, J.-S. McEwen, E.C.H. Sykes, Nat. Catal. 1 (2018) 192–198.

[95] L. Zhao, R. He, K.T. Rim, T. Schiros, K.S. Kim, H. Zhou, C. Gutierrez, S.P. Chockalingam, C.J. Arguello, L. Palova, D. Nordlund, M.S. Hybertsen, D.R. Reichman, T.F. Heinz, P. Kim, A. Pinczuk, G.W. Flynn, A.N. Pasupathy, Science 333 (2011) 999–1003.

[96] R.W. Carpick, M. Salmeron, Chem. Rev. 97 (1997) 1163–1194.

[97] Y. Cheng, S. He, S. Lu, J.-P. Veder, B. Johannessen, L. Thomsen, M. Saunders, T. Becker, R. De Marco, Q. Li, S.-Z. Yang, S.P. Jiang, Adv. Sci. 6 (2019), 1802066.

[98] H. Wei, X. Liu, A. Wang, L. Zhang, B. Qiao, X. Yang, Y. Huang, S. Miao, J. Liu, T. Zhang, Nat. Commun. 5 (2014) 5634.

[99] F. Yang, S. Ding, H. Song, N. Yan, Sci. China Mater. 63 (2020) 982–992.

[100] H.B. Yang, S.-F. Hung, S. Liu, K. Yuan, S. Miao, L. Zhang, X. Huang, H.-Y. Wang, W. Cai, R. Chen, J. Gao, X. Yang, W. Chen, Y. Huang, H.M. Chen, C.M. Li, T. Zhang, B. Liu, Nat. Energy 3 (2018) 140–147.

[101] Y. Pan, R. Lin, Y. Chen, S. Liu, W. Zhu, X. Cao, W. Chen, K. Wu, W.-C. Cheong, Y. Wang, L. Zheng, J. Luo, Y. Lin, Y. Liu, C. Liu, J. Li, Q. Lu, X. Chen, D. Wang, Q. Peng, C. Chen, Y. Li, J. Am. Chem. Soc. 140 (2018) 4218–4221.

[102] W. Cao, L. Lin, H. Qi, Q. He, Z. Wu, A. Wang, W. Luo, T. Zhang, J. Catal. 373 (2019) 161–172.

[103] M.J. Hülsey, B. Zhang, Z. Ma, H. Asakura, D.A. Do, W. Chen, T. Tanaka, P. Zhang, Z. Wu, N. Yan, Nat. Commun. 10 (2019) 1330.

[104] X. Liu, Y. Jiao, Y. Zheng, M. Jaroniec, S.-Z. Qiao, J. Am. Chem. Soc. 141 (2019) 9664–9672.

[105] Y.-Q. Su, Y. Wang, J.-X. Liu, I.A.W. Filot, K. Alexopoulos, L. Zhang, V. Muravev, B. Zijlstra, D.G. Vlachos, E.J.M. Hensen, ACS Catal. 9 (2019) 3289–3297.

[106] Y. Zhang, L. Jiao, W. Yang, C. Xie, H.-L. Jiang, Angew. Chem. Int. Ed. 60 (2021) 7607–7611.

[107] C. Cai, M. Wang, S. Han, Q. Wang, Q. Zhang, Y. Zhu, X. Yang, D. Wu, X. Zu, G.E. Sterbinsky, Z. Feng, M. Gu, ACS Catal. 11 (2021) 123–130.

[108] X. Lin, L. Li, X. Chang, C. Pei, Z.-J. Zhao, J. Gong, Sci. China Mater. 64 (2021) 1173–1181.

[109] C. Wang, S. Mao, Z. Wang, Y. Chen, W. Yuan, Y. Ou, H. Zhang, Y. Gong, Y. Wang, B. Mei, Z. Jiang, Y. Wang, Chem 6 (2020) 752–765.

[110] J. Hu, Y. Li, Y. Zou, L. Lin, B. Li, X.-y. Li, Chem. Eng. J. 437 (2022), 135428.

[111] X. Li, S. Wang, L. Li, Y. Sun, Y. Xie, J. Am. Chem. Soc. 142 (2020) 9567–9581.

[112] Y. Zeng, X. Li, J. Wang, M.T. Sougrati, Y. Huang, T. Zhang, B. Liu, Chem. Catal. 1 (2021) 1215–1233.

[113] L. Peng, X. Duan, Y. Shang, B. Gao, X. Xu, Appl. Catal. B Environ. 287 (2021), 119963.

[114] Y. Qi, J. Li, Y. Zhang, Q. Cao, Y. Si, Z. Wu, M. Akram, X. Xu, Appl. Catal. B Environ. 286 (2021), 119910.

[115] X. Duan, K. O'Donnell, H. Sun, Y. Wang, S. Wang, Small 11 (2015) 3036–3044.

[116] G. Liao, S. Chen, X. Quan, H. Yu, H. Zhao, J. Mater. Chem. 22 (2012) 2721–2726.

[117] K. Qian, H. Chen, W. Li, Z. Ao, Y.-n. Wu, X. Guan, Environ. Sci. Technol. 55 (2021) 7034–7043.

[118] Y. Gao, C. Yang, M. Zhou, C. He, S. Cao, Y. Long, S. Li, Y. Lin, P. Zhu, C. Cheng, Small 16 (2020), 2005060.

[119] S. Hoang, Y. Guo, A.J. Binder, W. Tang, S. Wang, J. Liu, H. Tran, X. Lu, Y. Wang, Y. Ding, E.A. Kyriakidou, J. Yang, T.J. Toops, T.R. Pauly, R. Ramprasad, P.-X. Gao, Nat. Commun. 11 (2020) 1062.

[120] J. Miao, Y. Zhu, J. Lang, J. Zhang, S. Cheng, B. Zhou, L. Zhang, P.J.J. Alvarez, M. Long, ACS Catal. 11 (2021) 9569–9577.

[121] Y. Zhang, Y. Liu, S. Xie, H. Huang, G. Guo, H. Dai, J. Deng, Environ. Int. 128 (2019) 335–342.

[122] X. Hao, L. Dai, J. Deng, Y. Liu, L. Jing, J. Wang, W. Pei, X. Zhang, Z. Hou, H. Dai, J. Phys. Chem. C 125 (2021) 17696–17708.

[123] X. Wang, H. Pan, M. Sun, Y. Zhang, J. Mater. Chem. A 10 (2022) 6078–6085.

[124] J. Wang, B. Li, Y. Li, X. Fan, F. Zhang, G. Zhang, W. Peng, Adv. Sci. 8 (2021), 2101824.

[125] F. Chen, X.-L. Wu, L. Yang, C. Chen, H. Lin, J. Chen, Chem. Eng. J. 394 (2020), 124904.

[126] N. Jiang, H. Xu, L. Wang, J. Jiang, T. Zhang, Environ. Sci. Technol. 54 (2020) 14057–14065.

[127] L.-Z. Huang, X. Wei, E. Gao, C. Zhang, X.-M. Hu, Y. Chen, Z. Liu, N. Finck, J. Lützenkirchen, D.D. Dionysiou, Appl. Catal. B Environ. 268 (2020), 118459.

[128] A. Svalova, V. Brusko, E. Sultanova, M. Kirsanova, T. Khamidullin, I. Vakhitov, A.M. Dimiev, Appl. Surf. Sci. 565 (2021), 150503.

[129] Y. Min, X. Zhou, J.-J. Chen, W. Chen, F. Zhou, Z. Wang, J. Yang, C. Xiong, Y. Wang, F. Li, H.-Q. Yu, Y. Wu, Nat. Commun. 12 (2021) 303.

[130] S. Zhao, Y. Wen, X. Liu, X. Pen, F. Lü, F. Gao, X. Xie, C. Du, H. Yi, D. Kang, X. Tang, Nano Res. 13 (2020) 1544–1551.

[131] K. Yang, Y. Liu, J. Deng, X. Zhao, J. Yang, Z. Han, Z. Hou, H. Dai, Appl. Catal. B Environ. 244 (2019) 650–659.

[132] Z. Hu, X. Li, S. Zhang, Q. Li, J. Fan, X. Qu, K. Lv, Small 16 (2020), 2004583.

[133] S. Chen, Y. Zhou, J. Li, Z. Hu, F. Dong, Y. Hu, H. Wang, L. Wang, K.K. Ostrikov, Z. Wu, ACS Catal. 10 (2020) 10185–10196.

[134] J. Pan, B. Gao, P. Duan, K. Guo, M. Akram, X. Xu, Q. Yue, Y. Gao, J. Mater. Chem. A 9 (2021) 11604–11613.

[135] J. Yang, D. Zeng, Q. Zhang, R. Cui, M. Hassan, L. Dong, J. Li, Y. He, Appl. Catal. B Environ. 279 (2020), 119363.

[136] Y. Gao, X. Duan, B. Li, Q. Jia, Y. Li, X. Fan, F. Zhang, G. Zhang, S. Wang, W. Peng, J. Mater. Chem. A 9 (2021) 14793–14805.

[137] J. He, Y. Wan, W. Zhou, J. Hazard Mater. 405 (2021), 124199.

[138] Y. Li, T. Yang, S. Qiu, W. Lin, J. Yan, S. Fan, Q. Zhou, Chem. Eng. J. 389 (2020), 124382.

[139] P. Cao, X. Quan, K. Zhao, S. Chen, H. Yu, Y. Su, Environ. Sci. Technol. 54 (2020) 12662–12672.

[140] J. Tian, D. Yang, J. Wen, A.S. Filatov, Y. Liu, A. Lei, X.-M. Lin, Nanoscale 10 (2018) 1047–1055.

[141] T. Xu, H. Zheng, P. Zhang, J. Hazard Mater. 388 (2020) 121746.

[142] Z. Mao, L. Liu, H.B. Yang, Y. Zhang, Z. Yao, H. Wu, Y. Huang, Y. Xu, B. Liu, Electrochim. Acta 391 (2021), 138886.

[143] A.H. Asif, N. Rafique, R.A.K. Hirani, H. Wu, L. Shi, S. Zhang, S. Wang, Y. Yin, M. Saunders, H. Sun, Chem. Eng. J. 432 (2022), 134429.

[144] P. Zhou, W. Ren, G. Nie, X. Li, X. Duan, Y. Zhang, S. Wang, Angew. Chem. Int. Ed. 59 (2020) 16517–16526.

[145] Y. Yao, H. Chen, J. Qin, G. Wu, C. Lian, J. Zhang, S. Wang, Water Res. 101 (2016) 281–291.

[146] Y. Yin, L. Shi, W. Li, X. Li, H. Wu, Z. Ao, W. Tian, S. Liu, S. Wang, H. Sun, Environ. Sci. Technol. 53 (2019) 11391–11400.

[147] J. Ma, Q. Yang, Y. Wen, W. Liu, Appl. Catal. B Environ. 201 (2017) 232–240.

[148] Q. Wu, J. Wang, Z. Wang, Y. Xu, Z. Xing, X. Zhang, Y. Guan, G. Liao, X. Li, J. Mater. Chem. A 8 (2020) 13685–13693.

[149] A. Fischbacher, J. von Sonntag, C. von Sonntag, T.C. Schmidt, Environ. Sci. Technol. 47 (2013) 9959–9964.

[150] X. Li, Y. Wang, J. Zhao, H. Wang, B. Wang, J. Huang, S. Deng, G. Yu, J. Hazard Mater. 300 (2015) 298–306.

[151] Z. Guo, Y. Xie, J. Xiao, Z.-J. Zhao, Y. Wang, Z. Xu, Y. Zhang, L. Yin, H. Cao, J. Gong, J. Am. Chem. Soc. 141 (2019) 12005–12010.

[152] L.-Z. Huang, C. Zhou, M. Shen, E. Gao, C. Zhang, X.-M. Hu, Y. Chen, Y. Xue, Z. Liu, J. Hazard Mater. 389 (2020), 122137.

[153] J. Xu, X. Zheng, Z. Feng, Z. Lu, Z. Zhang, W. Huang, Y. Li, D. Vuckovic, Y. Li, S. Dai, G. Chen, K. Wang, H. Wang, J.K. Chen, W. Mitch, Y. Cui, Nat. Sustain. 4 (2021) 233–241.

[154] N. Li, X. Song, L. Wang, X. Geng, H. Wang, H. Tang, Z. Bian, ACS Appl. Mater. Interfaces 12 (2020) 24019–24029.

[155] M. Lu, M. Liu, C. Xu, Y. Yin, L. Shi, H. Wu, A. Yuan, X.-M. Ren, S. Wang, H. Sun, Chin. J. Chem. Eng. (2021), https://doi.org/10.1016/j.cjche.2021.08.009.

[156] J. Kang, X. Duan, C. Wang, H. Sun, X. Tan, M.O. Tade, S. Wang, Chem. Eng. J. 332 (2018) 398–408.

[157] Q. Dong, H. Dong, Y. Li, J. Xiao, S. Xiang, X. Hou, D. Chu, J. Hazard Mater. 431 (2022), 128601-128601.

[158] X. Yu, Z. Gocze, D. Cabooter, R. Dewil, Chem. Eng. J. 404 (2021), 126403.

[159] Y. Yin, M. Liu, L. Shi, S. Zhang, R.A.K. Hirani, C. Zhu, C. Chen, A. Yuan, X. Duan, S. Wang, H. Sun, J. Hazard Mater. 435 (2022), 128939.

[160] X. Duan, H. Sun, Z. Ao, L. Zhou, G. Wang, S. Wang, Carbon 107 (2016) 371–378.

[161] X. Duan, H. Sun, Z. Shao, S. Wang, Appl. Catal. B Environ. 224 (2018) 973–982.

[162] H. Xu, N. Jiang, D. Wang, L. Wang, Y. Song, Z. Chen, J. Ma, T. Zhang, Appl. Catal. B Environ. 263 (2020), 118350.

[163] Y. Gao, Y. Zhu, T. Li, Z. Chen, Q. Jiang, Z. Zhao, X. Liang, C. Hu, Environ. Sci. Technol. 55 (2021) 8318–8328.

[164] D. Zhou, L. Chen, J. Li, F. Wu, Chem. Eng. J. 346 (2018) 726–738.

[165] H. Song, R. Du, Y. Wang, D. Zu, R. Zhou, Y. Cai, F. Wang, Z. Li, Y. Shen, C. Li, Appl. Catal. B Environ. 286 (2021), 119898.

[166] Q. Wang, H. Zeng, Y. Liang, Y. Cao, Y. Xiao, J. Ma, Chem. Eng. J. 407 (2021), 126738.

[167] H. Lee, H.-Y. Yoo, J. Choi, I.-H. Nam, S. Lee, S. Lee, J.-H. Kim, C. Lee, J. Lee, Environ. Sci. Technol. 48 (2014) 8086–8093.

[168] Y. Long, J. Dai, S. Zhao, Y. Su, Z. Wang, Z. Zhang, Environ. Sci. Technol. 55 (2021) 5357–5370.

[169] J. Zhang, Y. Li, X. Zhao, L. Wang, H. Chen, S. Wang, X. Xu, L. Shi, L.-C. Zhang, Y. Zhu, H. Zhang, Y. Liu, G. Nealon, S. Zhang, M. Wu, S. Wang, H. Sun, Nano Energy 89 (2021), 106357.

[170] A.H. Asif, S. Wang, H. Sun, Curr. Opin. Green Sustain. Chem. 28 (2021), 100447.

[171] X. Meng, L. Liu, S. Ouyang, H. Xu, D. Wang, N. Zhao, J. Ye, Adv. Mater. 28 (2016) 6781–6803.

[172] J.J. Rueda-Marquez, I. Levchuk, P.F. Ibanez, M. Sillanpaa, J. Clean. Prod. 258 (2020), 120694.

[173] L. Shi, Y. Yin, L.-C. Zhang, S. Wang, M. Sillanpää, H. Sun, Appl. Catal. B Environ. 248 (2019) 405–422.

[174] Q. Xu, L. Zhang, B. Cheng, J. Fan, J. Yu, Chem 6 (2020) 1543–1559.

[175] H. Park, Y. Park, W. Kim, W. Choi, J. Photochem. Photobiol., C 15 (2013) 1–20.

[176] W.-J. Ong, L.-L. Tan, Y.H. Ng, S.-T. Yong, S.-P. Chai, Chem. Rev. 116 (2016) 7159–7329.

[177] L. Zhou, H. Zhang, H. Sun, S. Liu, M.O. Tade, S. Wang, W. Jin, Catal. Sci. Technol. 6 (2016) 7002–7023.

[178] G. Wang, T. Zhang, W. Yu, R. Si, Y. Liu, Z. Zhao, ACS Catal. 10 (2020) 5715–5722.

[179] Z. Zeng, Y. Su, X. Quan, W. Choi, G. Zhang, N. Liu, B. Kim, S. Chen, H. Yu, S. Zhang, Nano Energy 69 (2020), 104409.

[180] Y. Yang, G. Zeng, D. Huang, C. Zhang, D. He, C. Zhou, W. Wang, W. Xiong, B. Song, H. Yi, S. Ye, X. Ren, Small 16 (2020), 2001634.

[181] F. Wang, Y. Wang, Y. Feng, Y. Zeng, Z. Xie, Q. Zhang, Y. Su, P. Chen, Y. Liu, K. Yao, W. Lv, G. Liu, Appl. Catal. B Environ. 221 (2018) 510–520.

[182] G. Chen, Y. Yu, L. Liang, X. Duan, R. Li, X. Lu, B. Yan, N. Li, S. Wang, J. Hazard Mater. 408 (2021), 124461.

[183] S. Zuo, X. Jin, X. Wang, Y. Lu, Q. Zhu, J. Wang, W. Liu, Y. Du, J. Wang, Appl. Catal. B Environ. 282 (2021), 119551.

[184] F. Chen, X.-L. Wu, C. Shi, H. Lin, J. Chen, Y. Shi, S. Wang, X. Duan, Adv. Funct. Mater. 31 (2021), 2007877.

[185] F. Wang, Y. Wang, Y. Li, X. Cui, Q. Zhang, Z. Xie, H. Liu, Y. Feng, W. Lv, G. Liu, Dalton Trans. 47 (2018) 6924–6933.

[186] L.F. Liotta, Appl. Catal. B Environ. 100 (2010) 403–412.

[187] V. Scholtz, J. Pazlarova, H. Souskova, J. Khun, J. Julak, Biotechnol. Adv. 33 (2015) 1108–1119.

[188] R. Zhou, R. Zhou, D. Alam, T. Zhang, W. Li, Y. Xia, A. Mai-Prochnow, H. An, E.C. Lovell, H. Masood, R. Amal, K.K. Ostrikov, P.J. Cullen, Chem. Eng. J. 403 (2021), 126413.

[189] H. Deng, S. Kang, J. Ma, L. Wang, C. Zhang, H. He, Environ. Sci. Technol. 53 (2019) 10871–10879.

[190] Y. Wang, H.-H. Liu, S.-Y. Wang, M.-F. Luo, J.-Q. Lu, J. Catal. 311 (2014) 314–324.

[191] C. Zhang, F. Liu, Y. Zhai, H. Ariga, N. Yi, Y. Liu, K. Asakura, M. Flytzani-Stephanopoulos, H. He, Angew. Chem. Int. Ed. 51 (2012) 9628–9632.

[192] Q. Dai, S. Bai, H. Li, W. Liu, X. Wang, G. Lu, Appl. Catal. B Environ. 168–169 (2015) 141–155.

[193] Z. Wang, S. Xie, Y. Feng, P. Ma, K. Zheng, E. Duan, Y. Liu, H. Dai, J. Deng, Appl. Catal. B Environ. 298 (2021), 120612.

[194] J. Pei, B. Peng, H. Lin, W. Chen, Y. Wang, J. Dong, J. Mao, D. Jia, W. Zhu, Z. Zhuang, ACS Appl. Mater. Interfaces 13 (2021) 53683–53690.

[195] J. Chen, L. Chen, X. Wang, Z. Rao, J. Sun, A. Chen, X. Xie, J. Colloid Interface Sci. 605 (2022) 674–684.

[196] H. Zhang, S. Sui, X. Zheng, R. Cao, P. Zhang, Appl. Catal. B Environ. 257 (2019), 117878.

[197] H. Zhang, X. Zheng, T. Xu, P. Zhang, ACS Appl. Mater. Interfaces 13 (2021) 17532–17542.

[198] X. Yang, X. Yu, M. Jing, W. Song, J. Liu, M. Ge, ACS Appl. Mater. Interfaces 11 (2019) 730–739.

[199] A. Mahmood, X. Wang, X. Xie, J. Sun, ACS Appl. Nano Mater. 4 (2021) 3799–3810.

[200] J. Lin, B. Qiao, N. Li, L. Li, X. Sun, J. Liu, X. Wang, T. Zhang, Chem. Commun. 51 (2015) 7911–7914.

[201] K. Fujiwara, S.E. Pratsinis, Appl. Catal. B Environ. 226 (2018) 127–134.

[202] Z. Wang, J. Zhao, J. Wang, C.R. Cabrera, Z. Chen, J. Mater. Chem. A 6 (2018) 7547–7556.

[203] S.H. Talib, S. Hussain, S. Baskaran, Z. Lu, J. Li, ACS Catal. 10 (2020) 11951–11961.

[204] G.S. Cooper, S. Jones, Environ. Health Perspect. 116 (2008) 1001–1008.

[205] M. Giedyk, R. Narobe, S. Weiß, D. Touraud, W. Kunz, B. König, Nat. Catal. 3 (2020) 40–47.

[206] E.T. Martin, C.M. McGuire, M.S. Mubarak, D.G. Peters, Chem. Rev. 116 (2016) 15198–15234.

[207] G. Jiang, X. Li, Y. Shen, X. Shi, X. Lv, X. Zhang, F. Dong, G. Qi, R. Liu, J. Catal. 391 (2020) 414–423.

[208] R. Liu, H. Zhao, X. Zhao, Z. He, Y. Lai, W. Shan, D. Bekana, G. Li, J. Liu, Environ. Sci. Technol. 52 (2018) 9992–10002.

[209] F. Hu, L. Leng, M. Zhang, W. Chen, Y. Yu, J. Wang, J.H. Horton, Z. Li, ACS Appl. Mater. Interfaces 12 (2020) 54146–54154.

[210] D. Huang, D.J. Kim, K. Rigby, X. Zhou, X. Wu, A. Meese, J. Niu, E. Stavitski, J.-H. Kim, Environ. Sci. Technol. 55 (2021) 13306–13316.

[211] O. Lugaresi, H. Encontre, C. Locatelli, A. Minguzzi, A. Vertova, S. Rondinini, C. Comninellis, Electrochem. Commun. 44 (2014) 63–65.

[212] Y. Peng, M. Cui, Z. Zhang, S. Shu, X. Shi, J.T. Brosnahan, C. Liu, Y. Zhang, P. Godbold, X. Zhang, F. Dong, G. Jiang, S. Zhang, ACS Catal. 9 (2019) 10803–10811.

[213] B. Liu, H. Zhang, Q. Lu, G. Li, F. Zhang, Sci. Total Environ. 635 (2018) 1417–1425.

[214] T. Liu, J. Luo, X. Meng, L. Yang, B. Liang, M. Liu, C. Liu, A. Wang, X. Liu, Y. Pei, J. Yuan, J. Crittenden, J. Hazard Mater. 358 (2018) 294–301.

[215] L.-Z. Huang, S.U. Pedersen, E.T. Bjerglund, P. Lamagni, M. Glasius, H.C.B. Hansen, K. Daasbjerg, Environ. Sci.: Nano 4 (2017) 2286–2296.

[216] Y. Xu, Z. Yao, Z. Mao, M. Shi, X. Zhang, F. Cheng, H.B. Yang, H.b. Tao, B. Liu, Appl. Catal. B Environ. 277 (2020), 119057.

[217] K.A.P. Payne, C.P. Quezada, K. Fisher, M.S. Dunstan, F.A. Collins, H. Sjuts, C. Levy, S. Hay, S.E.J. Rigby, D. Leys, Nature 517 (2015) 513–516.

[218] Z. Xiong, H. Zhang, W. Zhang, B. Lai, G. Yao, Chem. Eng. J. 359 (2019) 13–31.

[219] P. Zhao, X. Feng, D. Huang, G. Yang, D. Astruc, Coord. Chem. Rev. 287 (2015) 114–136.

[220] Q. Yan, X.-Y. Wang, J.-J. Feng, L.-P. Mei, A.-J. Wang, J. Colloid Interface Sci. 582 (2021) 701–710.

[221] Y. Xu, X. Shi, R. Hua, R. Zhang, Y. Yao, B. Zhao, T. Liu, J. Zheng, G. Lu, Appl. Catal. B Environ. 260 (2020), 118142.

[222] H. Qi, P. Yu, Y. Wang, G. Han, H. Liu, Y. Yi, Y. Li, L. Mao, J. Am. Chem. Soc. 137 (2015) 5260–5263.

[223] X.-k. Kong, Z.-y. Sun, M. Chen, C.-l. Chen, Q.-w. Chen, Energy Environ. Sci. 6 (2013) 3260–3266.

[224] Z. Hasan, D.-W. Cho, C.-M. Chon, K. Yoon, H. Song, Chem. Eng. J. 298 (2016) 183–190.

[225] V.K. Gupta, N. Atar, M.L. Yola, Z. Ustundag, L. Uzun, Water Res. 48 (2014) 210–217.

[226] J. Zhang, W. Geng, L. Shi, C. Yang, X. Zhang, Y. Geng, R. Arjan Kalyan Hirani, X. Xu, J. Wei, Y. Jing, S. Zhang, H. Zhang, S. Wang, H. Sun, Chem. Eng. J. 439 (2022), 135733.

[227] L. Liu, Y. Duan, Y. Liang, A. Kan, L. Wang, Q. Luo, Y. Zhang, B. Zhang, Z. Li, J. Liu, D. Wang, Small 18 (2022), 2104142.

[228] S. Guo, H. Yuan, W. Luo, X. Liu, X. Zhang, H. Jiang, F. Liu, G.J. Cheng, Nano Res. 14 (2021) 1287–1293.

[229] J. Li, L. Zhong, L. Tong, Y. Yu, Q. Liu, S. Zhang, C. Yin, L. Qiao, S. Li, R. Si, J. Zhang, Adv. Funct. Mater. 29 (2019), 1905423.

[230] C. Chen, W. Ou, K.-M. Yam, S. Xi, X. Zhao, S. Chen, J. Li, P. Lyu, L. Ma, Y. Du, W. Yu, H. Fang, C. Yao, X. Hai, H. Xu, M.J. Koh, S.J. Pennycook, J. Lu, M. Lin, C. Su, C. Zhang, J. Lu, Adv. Mater. 33 (2021), 2008471.

[231] L. Luo, J. Luo, H. Li, F. Ren, Y. Zhang, A. Liu, W.-X. Li, J. Zeng, Nat. Commun. 12 (2021) 1218.

[232] B. Li, C. Lai, G. Zeng, D. Huang, L. Qin, M. Zhang, M. Cheng, X. Liu, H. Yi, C. Zhou, F. Huang, S. Liu, Y. Fu, Small 15 (2019), 1804565.

[233] R. Feng, W. Lei, G. Liu, M. Liu, Adv. Mater. 30 (2018), 1804770.

[234] Y. Wang, X. Cui, J. Zhao, G. Jia, L. Gu, Q. Zhang, L. Meng, Z. Shi, L. Zheng, C. Wang, Z. Zhang, W. Zheng, ACS Catal. 9 (2019) 336–344.

[235] L. Shi, Y. Yin, S. Wang, H. Sun, ACS Catal. 10 (2020) 6870–6899.

[236] Y. Zhu, B. Zhang, X. Liu, D.-W. Wang, D.S. Su, Angew. Chem. Int. Ed. 53 (2014) 10673–10677.

[237] G. Liu, W. Jin, N. Xu, Angew. Chem. Int. Ed. 55 (2016) 13384–13397.

[238] H. Wu, X. Xu, L. Shi, Y. Yin, L.-C. Zhang, Z. Wu, X. Duan, S. Wang, H. Sun, Water Res. 167 (2019), 115110.

[239] N. Li, X. Lu, M. He, X. Duan, B. Yan, G. Chen, S. Wang, J. Hazard Mater. 414 (2021), 125478.

[240] X. Fang, J. Li, B. Ren, Y. Huang, D. Wang, Z. Liao, Q. Li, L. Wang, D.D. Dionysiou, J. Membr. Sci. 579 (2019) 190–198.

[241] K. Hu, W. Tian, Y. Yang, G. Nie, P. Zhou, Y. Wang, X. Duan, S. Wang, Water Res. 198 (2021), 117144.

[242] K. Hu, Y. Yang, Y. Wang, X. Duan, S. Wang, Chem. Catal. 2 (2022) 724–761.

[243] J. Kang, L. Zhou, X. Duan, H. Sun, Z. Ao, S. Wang, Matter 1 (2019) 745–758.

[244] T. Uekert, H. Kasap, E. Reisner, J. Am. Chem. Soc. 141 (2019) 15201–15210.

[245] M.C. Ariza-Tarazona, J.F. Villarreal-Chiu, J.M. Hernández-López, J. Rivera De la Rosa, V. Barbieri, C. Siligardi, E.I. Cedillo-González, J. Hazard Mater. 395 (2020), 122632.